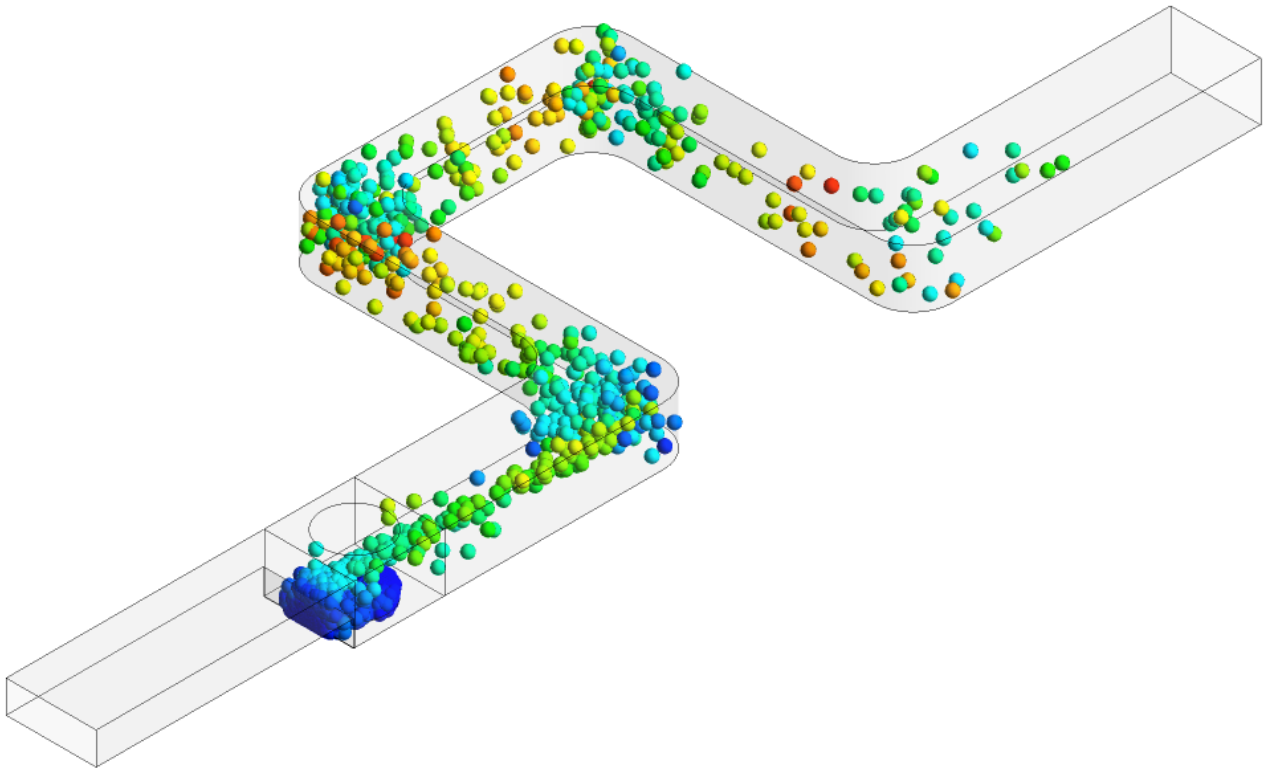




CHALMERS



CFD-DEM modeling of dry powder inhalers using micro-models

A numerical and experimental study

Master's thesis in Applied Mechanics

ELLY LUCIA GAGGINI
EMELIE WASBERG

MASTER'S THESIS IN APPLIED MECHANICS

CFD-DEM modeling of dry powder inhalers using micro-models

A numerical and experimental study

ELLY LUCIA GAGGINI
EMELIE WASBERG

Department of Mechanics and Maritime Sciences

Division of fluid dynamics

CHALMERS UNIVERSITY OF TECHNOLOGY

Göteborg, Sweden 2018

CFD-DEM modeling of dry powder inhalers using micro-models
A numerical and experimental study
ELLY LUCIA GAGGINI
EMELIE WASBERG

© ELLY LUCIA GAGGINI , EMELIE WASBERG, 2018

Master's thesis 2018:35
Department of Mechanics and Maritime Sciences
Division of fluid dynamics
Chalmers University of Technology
SE-412 96 Göteborg
Sweden
Telephone: +46 (0)31-772 1000

Cover:
Velocity of carrier particles emitting from a generic inhaler device.

Chalmers Reproservice
Göteborg, Sweden 2018

CFD-DEM modeling of dry powder inhalers using micro-models
A numerical and experimental study
Master's thesis in Applied Mechanics
ELLY LUCIA GAGGINI
EMELIE WASBERG
Department of Mechanics and Maritime Sciences
Division of fluid dynamics
Chalmers University of Technology

ABSTRACT

The continuous increase in computational power and the development of new particle models within Computational Fluid Dynamics (CFD) have made it feasible to use CFD as a complement to the physical testing in inhaler design. However, there are still challenges when simulating dry powder inhalers with carrier-based drug formulations due to the large number of fine active drug particles. An alternative approach is to model fine particles using so-called micro-models. These micro-models were coupled to a commercial CFD-DEM software that simulates the air flow and the carrier-particles. The micro-models describe the behaviour of fine particles in three different situations based on the dynamics of the carrier particle they are attached to. The first situation is the collision of a covered carrier particle against a wall causing the detachment of fine particles to the air and the attachment of fine particles to the wall. The second and third situations that cause detachment of fine particles are the collisions against other carrier particles and the drag force acting on the carrier particle exerted by the fluid flow. The fine particles detached into the air, follow the air flow and are tracked with a scalar transport equation. The mentioned modeling approaches were used to study two generic geometries loaded with a drug dose and with pressure drop and flow rate relevant for real inhalers. Experiments were performed on the two geometries and the CFD-DEM simulations were set up to mimic the experimental conditions by using the same flow rate and the same material properties of the drug formulation. Additional simulations were performed as sensitivity analyses. In the first sensitivity analysis, the effect of modeling the carrier particles using parcels compared to simulating them individually was studied. In the second sensitivity analysis the effect of the material properties of the drug dose was investigated by increasing the surface energy five times in the interaction between fine particles, carrier particles and walls. In the third sensitivity analysis the importance of the diffusive transport of fine particles was evaluated by increasing the diffusion coefficient. The results of the simulations showed that the implementation of micro-models was successful as the fine particles behaved as expected based on the dynamics of the carrier particles. The most important mechanism for the detachment of fine particles was the collisions of carrier particles against walls for both studied geometries. Further, the change in material properties, together with the design of the geometries, had a large effect on the results of the simulations, indicating that they must be taken into account concurrently to predict the performance of an inhaler device. The two geometries yielded a slight difference in results in terms of free fine particles emitted from the device in the numerical simulations. However, this difference was too small to be captured in the experiments, who also showed large variability in results between different tests.

Keywords: dry powder inhalers, computational fluid dynamics, micro-models, discrete element method, carrier-based drug formulation, ANSYS Fluent

ACKNOWLEDGEMENTS

This master's thesis work would not have been possible without the contribution of employees at the product development company Semcon and at Chalmers University of Technology. To begin with, we want to thank Sam Fredriksson, our supervisor at Semcon, for giving us the opportunity to work on this interesting project, for his support, guidance and dedication. We also want to thank our examiner at Chalmers University of Technology, Srdjan Sasic, for his valuable considerations, insights and expertise within the field of multiphase flows. Further, the time spent working with this master's thesis would not have been so great and stimulating without our excellent colleagues at Semcon, who gave us a warm welcoming, great company and generous sharing of knowledge. Among our colleagues at Semcon a special thanks is owed to Erik Sjösvärd for his helpfulness and enthusiasm. Finally, we want to thank AstraZeneca for the opportunity of performing experimental testings at their facilities.

NOMENCLATURE

Abbreviations

API	Active Pharmaceutical Ingredient
APS	Aerodynamic Particle Sizer
CFD	Computational Fluid Dynamics
DDPM	Dense Discrete Phase Model
DEM	Discrete Element Method
DPI	Dry Powder Inhaler
DPM	Discrete Phase Method
FFCE	Fraction of Fine particles attached to Carrier particles Emitted
FFCR	Fraction of Fine particles attached to Carrier particles Retained
FFE	Fraction of Fine particles Emitted
FFW	Fraction of Fine particles attached to Walls
LES	Large Eddy Simulation
lpm	liters per minute
MMAD	Mass Median Aerodynamic Diameter
RDF	Retained Dose Fraction
RSD	Relative Standard Deviation
UDF	User-Defined Function
USP	United States Pharmacopeia

Symbols

\mathbf{e}_{12}	unit vector between mass centers of colliding particles	
\mathbf{F}_{12}	contact force exerted by particle 1 on particle 2	[N]
$\mathbf{F}_{friction}$	contact force in tangential direction	[N]
\mathbf{F}_{fp}	fluid-particle interaction force	[N]
\mathbf{F}_{pp}	inter-particle forces	[N]
\mathbf{F}_{normal}	contact force in normal direction	[N]
\mathbf{F}_{vdw}	van der Waals force	[N]
\mathbf{g}	gravitational acceleration	[m/s ²]
H	Hamaker constant	
I	moment of inertia	[kgm ²]
K	spring constant	[N/m]
m	mass	[kg]
n_f	number of fine particles on a carrier particle	
$n_{f,init}$	initial number of fine particles on a carrier particle	
$n_{f,wall}$	number of fine particles attached to the wall	
p	pressure	[Pa]
S_ϕ	source term in scalar transport equation	[scalar/s/m ³]
\mathbf{T}	torque	[Nm]
\mathbf{u}_f	fluid velocity	[m/s]
\mathbf{u}_p	particle velocity	[m/s]
U_{vdw}	van der Waals interaction potential	[J]
\mathbf{v}	impact velocity	[m/s]
\mathbf{v}_r	relative velocity	[m/s]
\mathbf{v}_{12}	relative velocity between colliding particles	[m/s]
α_f	volume fraction of the fluid	
γ	surface energy	[J]
γ_{damp}	damping coefficient	[kg/s]
Γ	diffusion coefficient	[kg/(ms)]
δ	overlap	[m]
δ_0	minimum separation distance	[m]
μ	friction coefficient	
ρ_f	fluid density	[kg/m ³]
$\boldsymbol{\tau}$	viscous stress tensor	[Pa]
ϕ	scalar quantity	
$\boldsymbol{\omega}$	rotational velocity	[rad/s]

CONTENTS

Abstract	i
Acknowledgements	i
Nomenclature	iii
Contents	v
1 Introduction	1
1.1 Background	1
1.2 Aim	2
1.3 Scope	2
1.4 Thesis outline	2
2 Theory	3
2.1 Modeling of the fluid phase	3
2.2 Modeling of carrier particles	3
2.2.1 Particle-particle and particle-wall interaction	4
2.2.2 Parcels	5
2.3 Modeling of fine particles	5
2.3.1 Micro-models	6
2.3.2 Scalar transport equation	7
3 Methodology	9
3.1 Design of geometries	9
3.2 Simulations and analysis	10
3.2.1 Computational mesh study and meshing strategy	11
3.2.2 Solver settings in the CFD-DEM simulations	13
3.2.3 Modeling of fine particles	14
3.2.4 Overview of the simulations with particles	15
3.3 Experiments	17
3.3.1 Design and 3D-printing of the experimental devices	17
3.3.2 Experimental set-up, testing procedure and measurements	20
4 Results	23
4.1 Simulations	23
4.1.1 Overview of central notions concerning the results	23
4.1.2 Common results for the simulations	23
4.1.3 Base case simulations	26
4.1.4 Sensitivity analysis of the use of parcels	33
4.1.5 Surface energy	37
4.1.6 Diffusion	42
4.2 Experimental results	43
4.3 Comparison of numerical and experimental results	44
5 Discussion	47
5.1 Simulations	47
5.1.1 Base case simulations	47
5.1.2 Sensitivity analyses	48
5.1.3 Error sources	49
5.2 Experiments	50
5.2.1 Experimental error sources	50
5.3 Comparison of simulations and experiments	51
5.3.1 Limitations of the micro-models	51
5.4 Future work	52

6 Conclusions	53
References	54
A Measurements	I
B Experimental testing results	III

1 Introduction

The continuous increase in computational power and the development of new particle models within Computational Fluid Dynamics (CFD) have made it feasible to use CFD as a complement to physical testing in inhaler design. There are still, however, challenges regarding how to deal with large numbers of particles and how to model particle interaction. This chapter introduces the scope and context of this master's thesis. First, a background to the project is given, including a summary of previous work. Thereafter the aim, scope and key results of this work are presented. Finally, an outline of the report is given.

1.1 Background

Dry powder inhalers (DPIs) are extensively used within the pharmaceutical industry to deliver drugs to the lungs in medicinal applications. They consist of a drug formulation in the form of a dry powder and an inhalation device [1]. DPIs are advantageous since no propellant is needed and the drug formulation is kept in dry form, guaranteeing chemical stability and preventing bacterial proliferation [1] [2]. The drug particles need to be fine, smaller than $5\ \mu\text{m}$, in order to reach the lungs, since larger particles often settle in the upper airways. However, the adhesive forces between fine particles can be strong due to high surface energy, disturbing the flowability of the aerosol [2]. For this reason the fine drug particles are usually attached to larger inert carrier particles, covering their surface. During inhalation, the fine particles are desired to detach from the carrier particles, disperse into the air stream and finally reach the lungs [1].

To obtain correct and reliable drug dosing, both the dispersion of fine particles and the retention of particles in the device must be well-known. These aspects are affected simultaneously by the design of the device and by the formulation of the drug. The interaction between these two parameters is difficult to predict [1]. At the same time, achieving detailed results from experiments is difficult, especially regarding the interaction between carrier particles and fine particles [3]. Using the Discrete Element Method (DEM) coupled with CFD in numerical simulations, detailed information about the trajectory of each particle and the particle interaction can be obtained, which are difficult to attain from physical testing [4].

However, modeling DPIs with carrier-based formulations using CFD-DEM is challenging because of the large number of fine particles present in the system [2]. A drug dose of $1\ \text{mg}$ can contain around 10^9 fine particles, if the diameter is $1\ \mu\text{m}$, which is very expensive in terms of computational power. The same dosage containing carrier particles with a diameter of around $100\ \mu\text{m}$, would only consist of 1000 particles, which is feasible to simulate [1]. A possible approach is therefore to only simulate the carrier particles, not the fine particles, using DEM to save computational time. This allows to obtain detailed information about the behaviour of the carrier particles in inhaler devices. Nonetheless, to achieve reliable simulations a complementary modeling approach is needed for the fine particles.

Various papers have used a multi-scale modeling approach where they use DEM-simulations for the carrier particles and assume that the detachment and dispersion of fine particles depends on the dynamics of the carrier particles. The relationship between the dynamics of the carrier particles and the detachment of fine particles is determined by simulating a small number of carrier particles covered with fine particles. The results from these simulations are then used to formulate models, from now on referred to as micro-models, that describe the behaviour of fine particles as function of the dynamic properties of the carrier particles. These micro-models are then coupled with the CFD-DEM simulations of the fluid flow and carrier particles [1] [2]. This allows to develop models that can predict the quantitative behaviour of an inhaler device in the early stages of product development [1].

A study by Wachem et al. [1] presents a multi-scale modeling approach applied to a prototype inhaler. This multi-scale modeling is a combination of Large Eddy Simulation (LES) model of the fluid, DEM-modeling of the carrier particles and micro-models for the fine particles. The micro-models are functions of impact velocity and include four mechanisms: detachment of fine particles by particle-particle collisions, detachment of fine particles by particle-wall collisions, detachment of fine particles by fluid flow and re-attachment of fine particles to a carrier particle due to air flow.

To make these modeling approaches even more suitable for simulation driven product development, the models can be applied and coupled to common and well-proven commercial software that is used broadly in the industry. This has previously been done by Tong et al. [2], where the commercial CFD software ANSYS Fluent was used to solve the fluid flow. The solver was further coupled to a DEM code, which model the behaviour of the carrier particles, using User Defined Functions (UDFs) and the detachment of fine particles was modeled using micro-models. These micro-models are functions of the impact velocity and impact angle. They include detachment of fines upon particle-wall and particle-particle collisions.

To be able to use CFD modeling as a complement to physical testing in the product development of DPIs, it is desired to reduce the complexity of the modeling approaches. This can be achieved by using a commercial software not only for the CFD simulations, but also for the modeling of carrier particles with DEM. Further, the fine particles can be modeled by coupling micro-models to the commercial software.

1.2 Aim

The aim of this master's thesis is to investigate a computationally affordable way to apply CFD-DEM modeling to DPIs. This is done by modeling the fine particles with given micro-models that are implemented in the commercial CFD software ANSYS Fluent by using UDFs. The flow field is resolved using CFD and the dynamics of the carrier particles are modeled using DEM with adhesive forces included. Further, to evaluate the numerical modeling approaches, experimental testing is performed to be able to compare the numerical and experimental results.

1.3 Scope

The master's thesis is carried out at the product development company Semcon. Since the master's thesis focuses on the implementation of the micro-models and on evaluating the modeling approaches, the simulations are performed on two simplified generic geometries. These geometries are designed so to have a flow rate curve and a pressure drop relevant for real inhalers, but are not conceived to be similar to them in other aspects. The studied drug formulation consists of carrier particles coated with fine particles, for which the given micro-models are specifically developed. The micro-models describe the behaviour of fine particles covering a carrier particle as the carrier particle interacts with other carrier particles, walls and the fluid flow. The opportunity to perform physical testing at AstraZeneca's premises is given to compare the experimental results with the numerical simulations. In the comparison, the amount of fine particles emitted from the geometries and the retention are evaluated. Detailed analysis of turbulence modeling, DEM collision laws and solver settings are not part of the master's thesis as it focuses on the implementation and evaluation of the micro-models. The project is also constrained due to limited available computational power.

1.4 Thesis outline

This master's thesis report is relatively extensive, since the methodology and the results are presented quite thoroughly. The framework of the following chapters can briefly be explained as follows. Chapter 2 gives the relevant theoretical background to the master's thesis. Chapter 3 treats the methodology. First, the design of the two generic geometries is described. Then steps for setting up the numerical simulations are outlined, including solver settings, computational mesh independence study, implementation of micro-models and the cases simulated. Finally, the creation of 3D-printed devices for experimental testing and the experimental testing procedure are recounted. The results of the master's thesis are presented in Chapter 4. First, the complete results for the numerical simulations are described and then the experimental results for the 3D-printed devices are reported. Finally, the comparable results between numerical simulations and experiments are highlighted. In Chapter 5, results previously presented are analyzed and possible error sources are examined. Also future developments within the researched issues are suggested. Finally, the conclusions is given in Chapter 6. It includes a summary of important findings, their meaning and possible developments of the methodology used, with regards to the aim of the master's thesis.

2 Theory

In this chapter, relevant theoretical background for understanding the modeling approaches used in the Methodology, see chapter 3, is given. The chapter is divided into three parts. First, the modeling of the fluid phase using CFD is presented. Second, the theory behind the modeling of carrier particles is described. This includes tracking of the individual particles, particle-particle interaction, particle-wall interaction and the use of parcels. Third, the modeling of fine particles using micro-models and scalar transport equations is presented.

2.1 Modeling of the fluid phase

The motion of the fluid is governed by the Navier-Stokes equations in an Eulerian-framework. In CFD, the Navier-Stokes equations are averaged locally and solved in each computational cell. For multiphase flows with a high volumetric concentration of the discrete phase, the equations of the fluid phase need to be modified with the Dense Discrete Phase Model (DDPM) [5]. The Navier-Stokes equations can be written as [4]

$$\begin{aligned} \frac{\partial \alpha_f \rho_f}{\partial t} + \nabla \cdot (\alpha_f \rho_f \mathbf{u}_f) &= 0 \\ \frac{\partial \alpha_f \rho_f \mathbf{u}_f}{\partial t} + \nabla \cdot (\alpha_f \rho_f \mathbf{u}_f \mathbf{u}_f) &= -\alpha_f \nabla p - \mathbf{F}_{fp} + \nabla \cdot (\alpha_f \boldsymbol{\tau}) + \alpha_f \rho_f \mathbf{g}. \end{aligned} \quad (2.1)$$

The first equation above is the continuity equation of the fluid, where α_f is the volumetric fraction of the fluid, ρ_f is the density of the fluid and \mathbf{u}_f is the fluid velocity. The second equation is the momentum conservation equation, where p is the pressure, \mathbf{F}_{fp} is the fluid-particle interaction force, $\boldsymbol{\tau}$ is the viscous stress tensor and the last term is the gravitational force. The fluid-particle interaction force \mathbf{F}_{fp} is the sum of the fluid-particle interaction force $\mathbf{F}_{fp,i}$ in equation (2.2), of each particle i located in the computational cell [4].

When using CFD on turbulent or transitional flows, turbulence modeling is needed. One existing turbulence model is the $k - \epsilon$ model. It is a two-equation model that solves two transport equations: one for the turbulent kinetic energy k and one for its dissipation rate ϵ . The $k - \epsilon$ model has the advantage of being computationally cheap and robust and has been widely used in industrial applications for many types of flow. The realizable $k - \epsilon$ model is an improved $k - \epsilon$ model that performs better for complex flow with curved streamlines, rotation and separated flows [5].

Turbulence is affected by the presence of walls. Within CFD two different approaches exist for modeling turbulence close to the wall. The first one are wall functions, in which semi-empirical formulations are used to model the inner viscous region close to the wall. The second approach is the near-wall model approach in which the turbulence model is modified in order to resolve the fluid flow all the way down to the wall, including the viscous region. The two approaches have different requirements on the refinement of the computational mesh close to the wall. However, several wall treatments have been developed that combine the near-wall modeling with wall functions. The accuracy of these wall treatments is therefore less dependent on the characteristics of the mesh at the wall. One of these wall treatments available in Fluent for the $k - \epsilon$ turbulence model is the enhanced wall treatment [5].

2.2 Modeling of carrier particles

As previously mentioned, the formulation of a DPI consists of fine particles and carrier particles, where the carrier particles can be modeled using the Discrete Phase Model (DPM) in Fluent. In this model, the motion of a particle i is governed in an Lagrangian framework by Newton's second law of motion according to

$$\begin{aligned} m_i \frac{d\mathbf{u}_{p,i}}{dt} &= \mathbf{F}_{pp,i} + \mathbf{F}_{fp,i} + m_i \mathbf{g} \\ I_i \frac{d\boldsymbol{\omega}_i}{dt} &= \mathbf{T}_i \end{aligned} \quad (2.2)$$

where m_i , $\mathbf{u}_{p,i}$, $\boldsymbol{\omega}_i$ and I_i are the mass of particle i , the translational velocity, the rotational velocity and moment of inertia, respectively. On the right side of the equations above $\mathbf{F}_{pp,i}$, $\mathbf{F}_{fp,i}$, $m_i\mathbf{g}$ and \mathbf{T}_i are the particle-particle interaction force, the fluid-particle interaction force, the gravitational force and the total torque acting on the particle, respectively [2]. The particle trajectories are obtained by integrating equation (2.2) over time. The second equation accounts for the rotation of particles, which is pronounced for large and heavy particles [5]. For the particles in the studied case, this can therefore be neglected. To account for the particle-particle and particle-wall interactions, the Discrete Element Method (DEM) can be implemented in Fluent. The DEM accounts for the contact forces. The interaction forces are described in detail in section 2.2.1. The fluid-particle interaction force includes the forces acting on the particles generated by the surrounding fluid. This includes the drag force, the virtual mass force, the pressure gradient force, the thermophoretic force, the Brownian force, the Saffman's lift force and the Magnus lift force. Since the fluid considered is air, drag force is the dominant interaction force [4]. The virtual mass force and the pressure gradient force are proportional to the density ratio and are therefore negligible when considering solid particles in air. The thermophoretic force only needs to be included when large temperature gradients are present. Further, the Brownian force and Saffman's lift force are only recommended to be included for sub-micron particles. Finally, the Magnus lift force arises due to rotation of particles, which impact is pronounced for large, heavy particles [5].

2.2.1 Particle-particle and particle-wall interaction

Whenever particle-particle interaction is of importance, for example in flows with high volumetric concentration of the discrete phase, it is recommended to use DEM [5]. In particle-particle interaction, the acting forces consist of contact forces and possibly adhesive forces. The contact forces can be solved using DEM with the soft-particle approach proposed by Cundall and Strack [5] [6]. In the soft-particle approach the particles colliding are slightly overlapping with an overlap δ . This overlap is used to find the contact forces \mathbf{F}_{12} and \mathbf{F}_{21} , that are included in the term $\mathbf{F}_{pp,i}$ of equation (2.2). The contact forces and the overlap are illustrated in Figure 2.1.

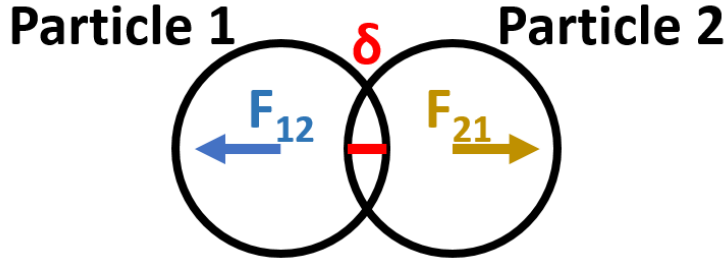


Figure 2.1: Illustration of the overlap δ between the colliding particles Particle 1 and Particle 2. \mathbf{F}_{12} is the contact force exerted by Particle 2 on Particle 1, and \mathbf{F}_{21} is the opposite.

The material properties of the particles determine the time step that can be used in the integration of equation (2.2). Several contact laws exist to model the contact forces, two of these are the spring-dashpot model and the friction collision law [5].

The spring-dashpot model is a contact law consisting of a linear spring force law and a dashpot term according to equation

$$\mathbf{F}_{12} = (K\delta + \gamma_{damp}(\mathbf{v}_{12} \cdot \mathbf{e}_{12})) \mathbf{e}_{12} \quad (2.3)$$

where K is the spring constant, δ is the overlap between the particles, γ_{damp} is the damping coefficient, \mathbf{v}_{12} is the relative velocity between the particles and \mathbf{e}_{12} is the unit vector between the mass centers of the particles [5]. The spring constant should be chosen so that the overlap is not too large compared to the particle diameter. The damping coefficient γ is a function of the restitution coefficient of the dashpot η . Further, Newton's third law yields that $\mathbf{F}_{12} = -\mathbf{F}_{21}$ [5].

The friction collision law models the tangential component of the contact force as a function of the friction coefficient and the normal component of the contact force. It is oriented in the direction opposite to the relative

tangential motion of the particle. It is based on the Coulomb friction according to

$$\mathbf{F}_{friction} = \mu \mathbf{F}_{normal} \quad (2.4)$$

where the friction coefficient μ is a function of the relative tangential velocity magnitude [5].

Depending on the physics of the studied system, adhesive forces may be a relevant component of the particle-particle interaction. Adhesive forces can be related to wetness, electrostatic charges and van der Waals forces. The van der Waals force is caused by the interaction of the molecules between solid surfaces and can cause particles to agglomerate [7]. For dry, non-charged particles, with a diameter smaller than 40 to 100 μm , which is a representative size for the carrier particles in this work, the van der Waals force should be taken into account [8]. The van der Waals force acting between spherical smooth particles can be written on the form

$$\mathbf{F}_{vdw} = -\nabla U_{vdw} \quad (2.5)$$

where U_{vdw} is the van der Waals interaction potential, which is a function of the Hamaker constant H , the surface-to-surface distance of the particles and the radii of the particles [8] [9]. The Hamaker constant is in turn a function of the material properties of the colliding particles. The surface energy of a spherical particle can be related to the Hamaker constant according to

$$\gamma = \frac{H}{24\pi\delta_0^2} \quad (2.6)$$

where H is again the Hamaker constant and δ_0 is the minimum separation distance [1] [10]. The van der Waals force \mathbf{F}_{vdw} in equation (2.5) acts between the centers of the particles. To avoid a nonphysical behaviour of the van der Waals force when particles are in contact, the increase of the force can be stopped when the surface-to-surface distance becomes smaller than a specified force-limiting distance [8].

The approaches described above to model particle-particle interaction are also valid for particle-wall interaction. Contact forces between a particle and a wall can be solved using DEM with the same contact laws as described in equations (2.3) and (2.4). Also the van der Waals force can act between a particle and a wall, causing the particle to attach to the wall. This behaviour is also modelled with equation (2.5). In the case of particle-wall interaction, the van der Waals forces is directed along the shortest distance between the particle and the wall, and the radius of the wall is considered to be infinite [8].

2.2.2 Parcels

The computational cost for tracking particles increases with increasing number of particles. To be able to model a large number of particles with limited resources, individual particles can be grouped into parcels. Using parcels with particles decreases the number of entities that are tracked, thereby decreasing the computational cost [11]. In this parcel model, all particles within a parcel are assumed to have the same properties, such as for example size and particle velocity [7]. The mass of a parcel is equal to the sum of the mass of all included particles. The volume of a parcel is determined as the mass of the parcel, divided by the particle density [5]. The computation of the parcel trajectory in a fluid flow is based on the volume of a single particle. On the other hand, the DDPM uses the parcel mass to calculate the volume fraction of the particulate phase. Further, it is also the parcel diameter and mass which are used to calculate the contact distance between parcels and forces in the DEM collision model. In order to fully represent the particle behaviour, enough parcels must be used. Hence, not too many particles can be grouped in each parcel to ensure a good statistical sample. Further, grouping fewer particles in each parcel often decreases problems with convergence, since no single parcel has a significant effect on the flow [11].

2.3 Modeling of fine particles

The available models for studying carrier particles described in section 2.2 cannot be implemented to the fine particles of a carrier particle based DPI, since the number of fine particles is too large. Therefore, micro-models have been developed to model the behavior of fine particles [1] [2]. In this work, the micro-models include the

detachment of fine particles upon collisions or due to drag force caused by the air flow and the attachment of fine particles to the walls upon particle-wall collisions. The micro-models are described in section 2.3.1. The fine particles detached into the air are tracked by introducing scalar transport equations, which are explained in section 2.3.2.

2.3.1 Micro-models

The given micro-models are based on DEM simulations and describe the behaviour of fine particles based on the dynamics of the carrier particles for three situations. To begin with, a carrier particle covered in fine particles can collide against another carrier particle or against a wall. During a collision fine particles can detach. Also, the carrier particles covered in fine particles are affected by the fluid phase through a drag force, which detach fine particles. The micro-models are developed for a formulation of carrier particles and fine particles with specific material properties. The detachment and attachment of fine particles in these micro-models are a function of the impact velocity and the surface energy, which is a simplification. In reality, the behaviour of fine particles depends on other particle properties as well, such as elasticity and friction. The micro-models in this work are presented below by first introducing the collision mechanisms and then drag dispersion.

Collisions

A carrier particle can collide against another carrier particle or against a wall. The fraction of fine particles that are detached from a carrier particle to the air upon a collision is given as

$$detached = \frac{n_{f,init} - n_f}{n_{f,init}} \quad (2.7)$$

where $n_{f,init}$ is the initial number of fine particles on the carrier particle and n_f is the number of fine particles left on the carrier particle. This fraction is formulated as a function of the magnitude of the impact velocity v on the form

$$detached = \begin{cases} A_0 v^{A_1}, & \text{if } v < A_2 \\ A_3 v^{A_4}, & \text{if } v \geq A_2 \end{cases} \quad (2.8)$$

where A_i are constants which depends on the surface energy of the drug formulation. In general, the larger the impact velocity and the lower the surface energy, the more fine particles are detached upon a collision.

Additionally for the particle-wall collisions, some fine particles covering the carrier particles can attach to the wall due to adhesive forces. The fraction of fine particles attached to the wall is modeled in a similar way, according to

$$attached = \frac{n_{f,wall}}{n_{f,init}} \quad (2.9)$$

where $n_{f,wall}$ is the number of fine particles attached to the wall. Also this fraction is formulated as a function of the impact velocity using equation (2.8), with different constants A_i which also depend on the surface energy of the drug formulation.

Drag dispersion

The surrounding fluid, in this case air, generates a drag force acting on the carrier particles. The fraction of fine particles which are detached due to the drag force is formulated as

$$detached = \begin{cases} A_0 v_r^{A_1} \Delta t, & \text{if } v < A_2 \\ A_3 v_r^{A_4} \Delta t, & \text{if } v \geq A_2 \end{cases} \quad (2.10)$$

where Δt is the length of the time step and v_r is the magnitude of the relative velocity between the fluid and the particle. As for equation (2.8), the constants A_i depends on the surface energy of the drug formulation. The relative velocity is defined as

$$\mathbf{v}_r = \mathbf{u}_f - \mathbf{u}_p \quad (2.11)$$

where \mathbf{u}_f is the fluid velocity and \mathbf{u}_p is the velocity of the carrier particle.

2.3.2 Scalar transport equation

For multiphase flows, the transport equation for a scalar ϕ in phase 1 is

$$\frac{\partial \alpha_1 \rho_1 \phi}{\partial t} + \nabla \cdot (\alpha_1 \rho_1 u_1 \phi - \alpha_1 \Gamma_1 \nabla \phi) = S_\phi \quad (2.12)$$

where α_1 is the local fluid volume fraction, Γ_1 is the diffusion coefficient of ϕ and S_ϕ is the source term. The equation describes the transport of the scalar ϕ in phase 1 due to convection and diffusion. The first term is the unsteady term, the second term is the convection term, the third term is the diffusion of scalar ϕ and the fourth term represents the source term of the scalar ϕ in phase 1 [5]. In this master's thesis the scalar ϕ represents the number of fine particles dispersed in the air flow.

3 Methodology

In this chapter, the methodology of this master’s thesis is described. As mentioned in section 1.2, the aim was to implement the modeling approaches presented in chapter 2, i.e. CFD-DEM modeling of fluid flow and carrier particles together with micro-models describing the fine particles, on a generic inhaler device. Since the opportunity to perform experimental testing was given in the project, the ambition was to compare the results of the simulations with the results of the experiments. For this reason, the numerical simulations were designed to mimic the experiments. As part of the assessment of the micro-models and their implementation, two relevant properties were compared in the experiments and in the simulations. These properties were the fraction of fine particles emitted from the device and the retention of particles in the device. The execution of this work consisted of three parts that are described in this chapter. The first part is the design of the generic inhaler devices, which were later used in the numerical simulations and in the experiments. Thereafter, the methodology of the numerical simulations and analyses is presented. Finally, the experimental preparation and testing procedure are described.

3.1 Design of geometries

Two geometries, which represent the fluid domains, were designed in SpaceClaim to be used in the simulations and experiments. The aim of the design was to find two geometries which would yield different results in terms of fine particles emitted from the device. The same geometries were used in the simulations and the experiments to be able to compare the results. Hence, the aim was not to perfectly mimic a real inhaler. Instead generic geometries were used with some properties similar to real inhalers, to make the conclusions applicable to inhalers. Therefore, it was decided that both geometries should yield a pressure drop within the interval of 2 to 4 kPa for a flow rate of 40 liters per minute (lpm). Further, it was decided to include a backwards facing step close to the inlet, to create a re-circulation region that could lift the particles and ease the visualization of the drug powder in the experiments.

In order to achieve different results in terms of emitted fine particles, the number of fine particles which detached from the carrier particles needed to be different for the two geometries. This was achieved by creating two geometries where the number of collisions and velocities of the particles were different in comparison. Therefore, it was decided that the geometries should include a different number of bends. One geometry includes one bend and is hereafter referred to as L-bend. Including only one bend should minimize the number of particle-wall and particle-particle collisions. The other geometry was decided to have four bends, which should increase the number of collisions significantly. This geometry is hereafter called Ω -bend. After the general features were determined for the two geometries, a trial and error procedure was performed to find the dimensions of the geometries which gave the desired pressure drop. Both the dimensions of the cross-section and the length of the different parts in the flow direction were varied until the desired pressure drop was achieved. The pressure drops were obtained by doing preliminary simulations of the air flow through the two geometries. The two final geometries can be seen in Figure 3.1 and the measurements of the geometries can be found in Appendix A. For the L-bend, the inlet has the dimensions 1.5 mm \times 7 mm and can be seen, together with the outlet, in Figure 3.1a. The height of the inlet increases to 2 mm shortly before the backwards facing step. Figure 3.1b shows the inlet, which has the dimensions 2.5 mm \times 7 mm and the outlet for the Ω -bend.

In Figure 3.1, the indentation close to the backwards facing step can be seen. The indentation was added to indicate where the drug dose should be placed, both in the simulations and the experiments. It also helped keeping the drug in place during handling of the device in the experimental testing. The indentation was added after the number of bends and the dimensions of the two geometries were determined. Preliminary simulations showed that the indentation could not be too deep: when the indentation was made deeper, more carrier particles collided with the walls of the indentation, causing a lot of fine particles to detach. This was not desired since the number of collisions should be minimized for the L-bend. Therefore, the indentation was made 0.25 mm deep. Further, the bottom of the indentation has a diameter of 4.5 mm.

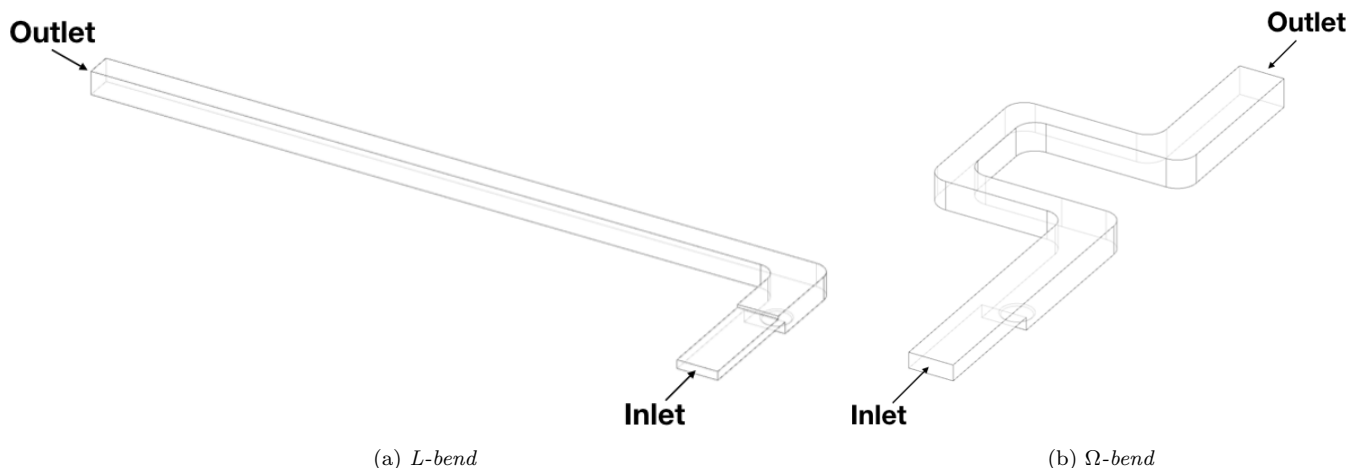


Figure 3.1: *The geometries used in the simulations and the experiments.*

The walls of the indentation could not be made too steep, since that could possibly prevent the drug dose from being released into the domain. Thus, the walls of the indentation have an inclination of 45° . The top of the indentation therefore had a diameter of 5 mm. A close-up of the indentation can be seen in Figure 3.2.

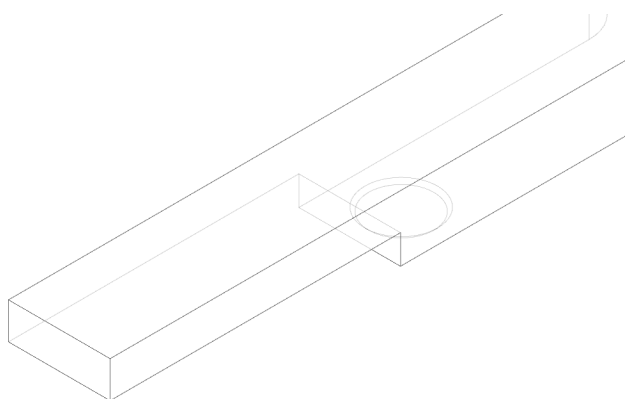


Figure 3.2: *Close-up of the indentation of the Ω -bend.*

3.2 Simulations and analysis

The work for setting up the simulations consisted of several steps that is presented in this section. A mesh study was performed to identify the computational mesh that gave good accuracy in the results, while meeting requirements of computational affordability. This is the first part presented in this section. Second, the settings of the CFD-DEM solver are described, which was used to model the fluid phase and the carrier particles. After that, the modeling of fine particles using micro-models and scalar transport equations is described. Finally, an overview of the simulations is given at the end of this section.

In the simulations, the two geometries mentioned in section 3.1 were simulated with an inflow of air and a drug dose positioned in the geometry. The drug dose consisted of a specific amount of carrier particles covered with 2000 fine particles. The carrier particles were considered to be mono-sized spheres with a diameter in the order 10-100 μm . The fine particles have a diameter in the order of 1 μm . The mass ratio of a fine particle and a carrier particle is 1 to 50 000.

3.2.1 Computational mesh study and meshing strategy

Lagrangian particle tracking has the requirement that the cell size of the computational mesh should be larger than the particle diameter **KÄLLA**. At the same time, in order to resolve the fluid flow, the mesh must be refined. These demands are conflicting, so a meshing strategy to find the coarsest mesh that give acceptable accuracy in the results was investigated. This meshing strategy was then used to create the meshes used for the simulations on the final geometries. The computational mesh independence study was performed on one geometry, the Ω -bend. Since it was done in an early stage of the project, the Ω -bend used, from now on referred to as preliminary Ω -bend, was not the geometry used in the simulations and experiments. It is very similar in terms of shape and measurements, but has no indentation. The preliminary Ω -bend can be seen in Figure 3.3 and the measurements of the geometry can be found in Appendix A.

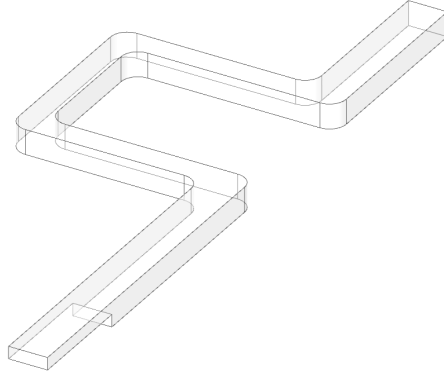


Figure 3.3: *Isometric view of the preliminary Ω -bend geometry used in the computational mesh study.*

The dimensions of the inlet, the face closest to the viewer, are $2.25 \text{ mm} \times 7.5 \text{ mm}$. The height of the geometry is 4.5 mm and the width is 7 mm in the wider sections and 4.5 mm in the thinner sections. The mesh study was only performed on the fluid phase, without carrier particles, for a constant inlet velocity of 47 lpm . All meshes tested had hexahedral elements. The solver settings were steady state with default discretization schemes and under-relaxation factors. The turbulence model used was realizable $k - \epsilon$ with enhanced wall treatment, the same as in the simulations. Two parameters were investigated in the computational mesh independence study: the smallest length of a cell side as a constant times the diameter of a carrier particle and the ratio between the largest and the smallest cells, called bias factor. The smallest length of the cell side was controlled by setting the number of divisions on the edges of the geometry. This strategy was mainly applied to the edges orthogonal to the flow direction and to the bends. In the flow direction, the constraint of a maximum cell size was applied. The values of the maximum cell size was chosen so to limit the total number of cells to below $512\,000$, due to restrictions of the software licenses used. The skewness of the computational cells was low in all the meshes tested. The variable evaluated in the mesh independence study was the decrease in static pressure between the inlet and the outlet. The value of the static pressure decrease and the residuals of the simulation were qualitatively compared at each iteration to ensure that the solution converged for each mesh tested. The meshes tested and their characteristics can be seen in Table 3.1.

Table 3.1: Characteristics of the meshes used in the computational mesh study, where d_p is the diameter of a carrier particle.

Mesh nr	Minimum cell length / d_p	Bias factor	Number of cells
1	1	4	510 384
2	1.5	2	509 208
3	1.5	4	210 438
4	2	2	255 552
5	2	4	103 488
6	3	1	147 200
7	3	1.5	94 208
8	3	2	72 128

The results for the different meshes were compared with the results for the finest mesh, i.e. mesh number one in Table 3.1. The percent difference of the static decrease between mesh number one and the coarser meshes can be seen in Figure 3.4.

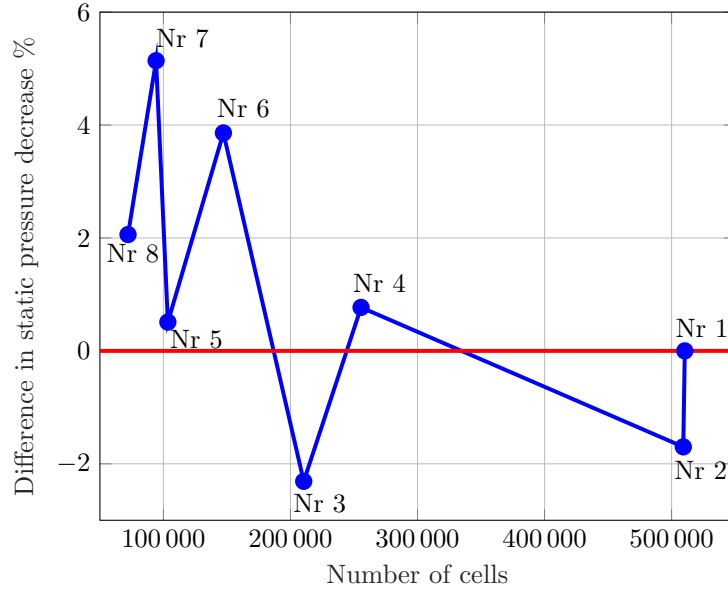


Figure 3.4: The percent difference in static pressure decrease between the finest mesh, mesh number 1, and the other meshes in the mesh study, plotted over the number of elements. Each value is labeled with the corresponding mesh number. The red horizontal line marks the value of 0 % in static pressure drop difference.

Mesh number four was considered to be the best compromise between the incompatible requirements, since it only had a relative difference in static pressure decrease of 0.77 % compared to the finest mesh, the residuals converged smoothly and the minimum cell size was twice the diameter of a carrier particle. It had a maximum cell size in the flow direction equal to 0.35 mm. Mesh number five had lower difference in static pressure decrease, but also fewer elements compared to mesh number four. This indicates that the flow field would not be as well resolved as for mesh number four if it were to be used in the simulations.

The meshing strategy used when meshing the L-bend and the Ω -bend in the simulations was mostly the same as for mesh number four in the mesh study. One difference was that the maximum cell size in the flow direction could be reduced to 0.28 mm instead of 0.35 mm, since the volumes of the final geometries were smaller.

The number of cells is 213 576 in the mesh for the L-bend and 187 200 in the mesh Ω -bend. The mesh densities of the geometries are 77.62 cells per mm^3 for the L-bend and 59.53 cells per mm^3 for the Ω -bend. The Ω -bend have a lower mesh density because of the middle part that is only 4 mm wide. This limits the number of division possible for the mesh over the width of the fluid domain in order to not have cell sizes smaller than twice the carrier particle diameter.

The L-bend and the Ω -bend have a circular indentation on the bottom close to the inlet (see section 3.1). In order to mesh that area correctly a new mesh strategy was applied to that part of the fluid domain. Zoomed in views of this zone for the Ω -bend mesh can be seen in Figure 3.5.

The outer circle in Figure 3.5a is where the indentation connects to the rest of the fluid domain, which can also be seen in Figure 3.5b. The requirement that all cells should be larger than twice the carrier particle diameter could not be fulfilled in the central square region. In order to have a good mesh with appropriate refinement in the rest of the fluid domain, the minimum cell size in the inner square region is one particle diameter. In this way the mesh connected smoothly between the indentation and the rest of the fluid domain.

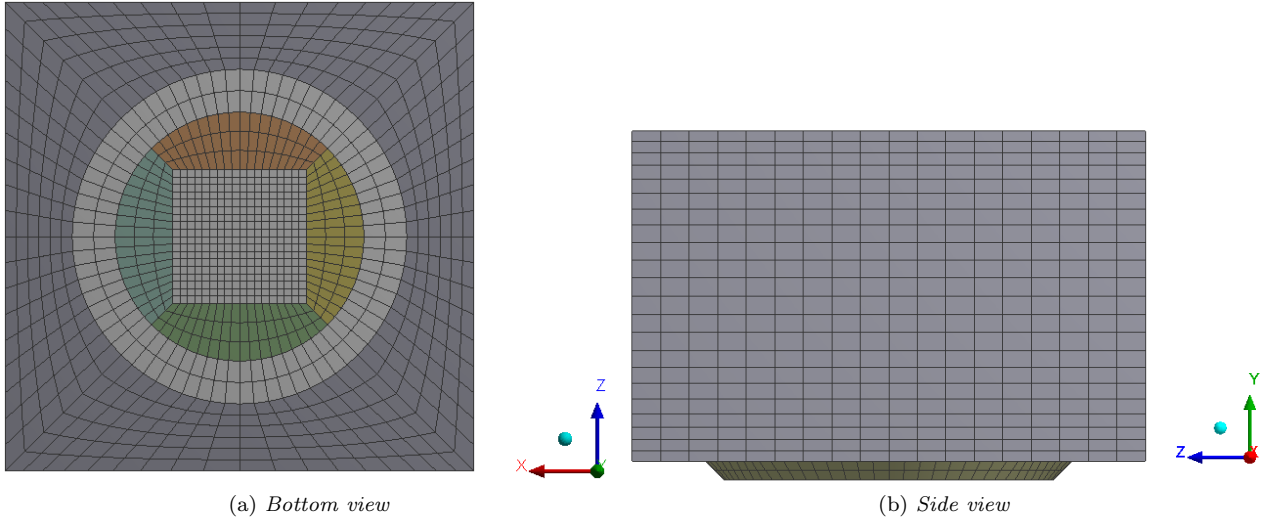


Figure 3.5: Views of the mesh of the fluid domain for the Ω -bend where the indentation is located.

3.2.2 Solver settings in the CFD-DEM simulations

The simulations in this work handles a multiphase problem, since both an air flow and a discrete phase were present. For this reason Eulerian-Lagrangian modeling was used, in which the fluid phase is solved using CFD and the discrete phase is solved using DEM. For details about CFD and DEM modeling, see chapter 2.

In the CFD solver, the Navier-Stokes equations were solved numerically by the software in order to describe the flow field of air in the geometries. DDPM was applied to the mass and momentum equations of the fluid in order to account for the volume fraction of the discrete phase. The turbulence in the flow field was resolved using the realizable $k - \epsilon$ model with enhanced wall treatment. The discretization schemes used were phase coupled simple as pressure-velocity coupling, Green-Gauss node based discretization for the gradients and the QUICK scheme for momentum, volume fraction, turbulent kinetic energy and turbulent dissipation rate. The chosen transient formulation was first order implicit. In order to ease convergence of the solution, under-relaxation factors were applied to pressure, momentum, turbulent kinetic energy and turbulent dissipation rate. The particle time step was taken as significantly smaller than the fluid time step. The fluid phase and the discrete phase were coupled with two-way coupling. In this approach, they affected each other through momentum exchange mechanisms [5].

The boundary conditions of the fluid phase were set as follows. The inlet velocity was set as a function of time, based on the flow rate according to

$$v_{in} = \frac{Q}{A} \quad (3.1)$$

where v_{in} is the inlet velocity, Q is the flow rate and A is the area of the inlet. To match the experiments, a maximum flow rate of 40 lpm was used for both geometries. The flow rate is a function of time, which was determined based on the rise time obtained in the experiments. The rise time is defined as the time it takes for the flow rate to reach 90 % of its maximum value, in this case 40 lpm. The curve for the flow rate used in the numerical simulations can be seen in Figure 3.6. As can be seen, linear relationships were assumed between the flow rate and time. In Figure 3.6 it can be seen that the rise time for the L-bend is longer than for the Ω -bend. Since the L-bend has a longer rise time, it took longer time for the velocity to reach its maximum value. Further, the inlet area is smaller for the L-bend, which resulted in a higher maximum inlet velocity for the L-bend compared to the Ω -bend.

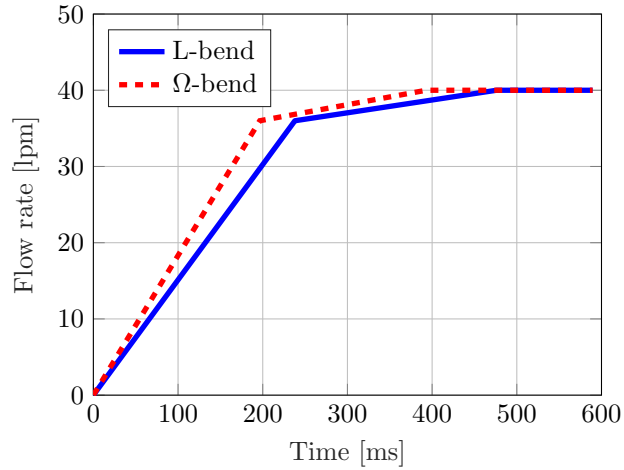


Figure 3.6: *The flow rate over time for the L-bend and the Ω -bend used in the numerical simulations.*

The inlet velocity profile can be seen in Figure 3.7.

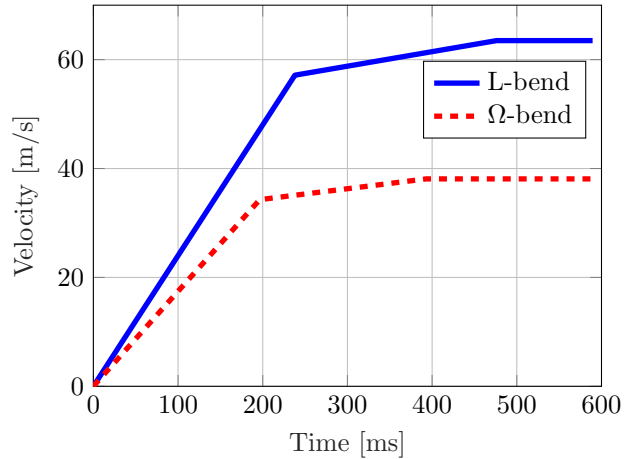


Figure 3.7: *The inlet velocity for the L-bend and the Ω -bend used in the numerical simulations.*

The outlet was set as pressure-outlet and the walls were treated as stationary. The standard wall roughness model was used with a roughness constant of 0.5, which was default in the solver. For the carrier particles, the inlet and the outlet were set as escape conditions. The walls for the DEM solver were set as a reflect boundary condition with the same contact laws and coefficients as for particle-particle collision, including adhesion, as described previously in chapter 2.

3.2.3 Modeling of fine particles

Micro-models were used to model the detachment of fine particles for three situations: particle-particle collisions, particle-wall collisions and dispersion of fine particles due to drag force acting on the carrier. These micro-models were implemented through User-Defined Functions (UDFs) into Fluent, to extend the capabilities of the solver. The micro-models implemented in the UDFs were coupled to the solver and therefore needed information about the flow field and particle variables (see equations (2.8) and (2.10)). This information was passed from the solver at each particle time step. The fine particles were assumed to not affect the flow or the carrier particles, and therefore a one-way coupling was used with regard to the fine particles.

The fine particles were modeled in two complementing ways. The fraction of fine particles detached into the air obtained from each micro-model were given as a source term S_γ in the three scalar transport equations,

see section 2.3.2. Each scalar transport equation tracks the fine particles dispersed in air, detached due to each mechanism. The fine particles, modeled as scalars, follow the fluid flow and exit the geometries through the outlet, which corresponds to the fine particles being emitted. The three scalar transport equations were used to compare the importance of each mechanism for detachment of fine particles. Second, the number of fine particles still left on the carrier particles and the number of fine particles which attached to the walls upon particle-wall collisions were tracked throughout the simulations. The following two sections describe the implementation of the micro-models for collisions and dispersion due to drag force, respectively.

Collisions

The particle-particle and particle-wall collisions were solved by the solver Fluent using the DEM collision model described in section 2.2.1. However, the collisions needed to be identified within the UDFs in order to implement the micro-models. When a collision was identified, the micro-models were used to update the number of fine particles left on that specific carrier particle, the number of fine particles that attached to the wall and the fraction of fine particles that was detached into the air. The latter was given to the scalar transport equations as a source term so that the fines dispersed in air could be tracked. The micro-models are functions of the impact velocity, see equation (2.8). For a particle-wall collision, the impact velocity was taken as the wall normal velocity. For a particle-particle collision, it was taken as the relative velocity of the colliding carrier particles.

Further, to be able to compare the importance of particle-particle collisions and particle-wall collisions, respectively, the collision energy was calculated for each collision. The collision energy was defined as the kinetic energy, calculated with the impact velocity used in the micro-models.

Drag dispersion

The drag force acting on the carrier particles continuously pulled away fine particles. This mechanism was modelled using equation (2.10) and depends on the relative velocity between the fluid and the carrier particle. It was updated each particle time step in order to use the most accurate velocities. The fine particles that were detached into the air were added as a source term to one of the scalar transport equations.

3.2.4 Overview of the simulations with particles

The numerical simulations with particles can be divided into two parts, which are presented below. The first part consists of two simulations, one for each geometry, which were set up to mimic the experiments. These two simulations will be referred to as base cases from now on. The second part includes three sensitivity analyses for each geometry: First, a comparison of modeling the carrier particles as individual particles or as parcels with particles. Second, an analysis of the importance of the value of the surface energy. Third, an analysis of the influence of the value for the diffusion coefficients in the scalar transport equations. The result of the sensitivity analyses were used to evaluate the results of the base cases and the experiments. For all cases, the solver settings were the same as described in section 3.2.2. All cases are summarized in Table 3.2 for the L-bend and 3.3 for the Ω -bend. In addition, two simulations, one for each geometry, including only the fluid flow, hence without particles, were run to investigate the flow field.

Table 3.2: Description of the cases for the simulations using L-bend. For the cases including parcels, each parcel includes 10 particles.

Name	Use of parcels	Number of particles	Description
L-Base	Yes	25 000	To be compared with the experiments
L-Particles	No	1000	Sensitivity analysis of the use of parcels
L-Parcels	Yes	1000	Sensitivity analysis of the use of parcels
L-Particles2	No	10 000	Sensitivity analysis of the use of parcels
L-Parcels2	Yes	10 000	Sensitivity analysis of the use of parcels
L-Hamaker	Yes	25 000	Sensitivity analysis of the surface energy
L-Diffusion	Yes	25 000	Sensitivity analysis of the diffusion coefficients

Table 3.3: Description of the cases for the simulations using Ω -bend. For the cases including parcels, each parcel includes 10 particles.

Name	Use of parcels	Number of particles	Description
Ω -Base	Yes	25 000	To be compared with the experiments
Ω -Particles	No	1000	Sensitivity analysis of the use of parcels
Ω -Parcels	Yes	1000	Sensitivity analysis of the use of parcels
Ω -Hamaker	Yes	25 000	Sensitivity analysis of the surface energy
Ω -Diffusion	Yes	25 000	Sensitivity analysis of the diffusion coefficients

A surface energy of $3.6 \times 10^{-3} \text{ J/m}^2$ was used in the simulations. The value of the surface energy affects the adhesion of carrier particles to each other and to walls. It also affects the fraction of fine particles attached to walls and detached upon collisions or due to drag force. The value of the surface energy is represented by the values of the constants in the micro-models, according to equations (2.8) and (2.10), as the constants are specific for the surface energy and other material properties of the drug formulation. Further, the diffusion coefficients in the scalar transport equations were taken as $1 \times 10^{-6} \text{ kg/(ms)}$.

Base case simulations

Two cases, one for each geometry, were designed to mimic the experiments, so that a comparison of the results could be made. Therefore, a large number of carrier particles was used. Since the modeling approach of using parcels was considered to be the most affordable, 2500 parcels were used with 10 carrier particles in each. This corresponded to 25 000 carrier particles covered in fine particles with a total weight of 7.1 mg, which is similar to a dose that could be used in the experiments. The simulations were initialized with the parcels in a cylindrical structure on the bottom of the indentation, with a distance of 20 % of the parcel diameter between them in all directions. These two simulations are from now on referred to as L-Base and Ω -Base.

Sensitivity analysis of the use of parcels

In the experimental part of the study, a standard dose weighted around 5 to 10 mg. This corresponds to approximately 18 000 to 35 000 carrier particles covered with fine particles. In the numerical simulations, this requires a large amount of computational power. In order to save computational effort, individual carrier particles were grouped into parcels. Using parcels containing 10 carrier particles each, means that only 1800 to 3500 entities need to be tracked individually in the simulations.

To ensure that grouping 10 carrier particles in a parcel would give reliable and accurate results, a sensitivity analysis was performed. In the sensitivity analysis, 1000 carrier particles were simulated using both approaches for both geometries: one case with 1000 individual carrier particles and another case with 100 parcels each containing 10 carrier particles. The two simulations with 1000 individual carrier particles, from now on referred to as L-Particles and Ω -Particles, were initialized with the 1000 carrier particles in a cubic structure at the bottom of the indentation. The initial distance between the carrier particles was set to 20 % of the carrier particle diameter, in all directions. For the two simulations with 1000 carrier particles in 100 parcels, from now on referred to as L-Parcels and Ω -Parcels, also the parcels were initially placed in a cubic structure at the bottom of the indentation. The parcels were placed so that the center of the outer parcels had the same coordinates as the center of the outer particles in the cases L-Particles and Ω -Particles, respectively.

To further investigate if parcels could be used for the studied cases, a second run of simulations was done for the L-bend geometry. These two cases included 10 000 carrier particles, from now on referred to as L-Particles2, and 10 000 carrier particles grouped in 1000 parcels, from now on referred to as L-Parcels2. The carrier particles and parcels were injected and initialized in the same way as for L-Particles and L-Parcels, respectively.

Sensitivity analysis of the surface energy

A sensitivity analysis of the surface energy was also conducted. The value of the surface energy of the drug formulation used in the experiments was considered to be a factor of uncertainty. It was assumed that the value

of the surface energy could affect the results of the base cases significantly and thereby also the comparison with the experiments. The value of the surface energy was increased with a factor of 5 to $1.8 \times 10^{-2} \text{ J/m}^2$. This corresponds to an increase of the Hamaker constant from 4.3×10^{-20} to 2.2×10^{-19} . The simulations with the higher value of the Hamaker constant were called L-Hamaker and Ω -Hamaker.

Sensitivity analysis of the diffusion coefficients

Further, also the diffusion coefficients used in the three scalar transport equations, see Γ in equation (2.12), were investigated. The diffusion transport mechanism was assumed to be negligible compared to convection for the dispersion of fine particles. Therefore, a small value for the diffusion coefficients was used in the base cases, but in order to quantify the effect of an increase of the diffusion coefficients on the solution, simulations with a value of 10^{-3} kg/(ms) were run. This corresponds to an increase of three magnitudes compared to what was used in the base cases. The simulations with a higher value for the diffusion coefficients are from now on referred to as L-Diffusion and Ω -Diffusion. Changing the values of the diffusion coefficient for the scalar transport equations only affect the results for the transport of fine particles. Hence, this sensitivity analysis did not influence the result of the fluid flow or the carrier particles.

3.3 Experiments

As a complement to the numerical simulations, experimental testing of 3D-printed devices was carried out on the premises of AstraZeneca. The aim with the experiments was to compare them with the simulations to evaluate the implementation of the micro-models. For this reason the solver set-up and the experimental set-up were designed to mimic each other. In this section the creation, 3D printing and after-treatment of the physical devices are described, as well as the experimental set-up, the testing procedure and the measurements performed.

3.3.1 Design and 3D-printing of the experimental devices

The devices, one for the L-bend and one for the Ω -bend, were created from the CAD-models of the fluid domains used in the numerical simulations (see Figure 3.1), by adding walls and other features. Each device consists of three different parts that were assembled. Even if the parts for the L-bend device and the Ω -bend device have different dimensions, the common general features can be described as follows. The bottom part of each device, denoted as part one, is the main part of the body and can be seen in Figure 3.8 for the two devices.

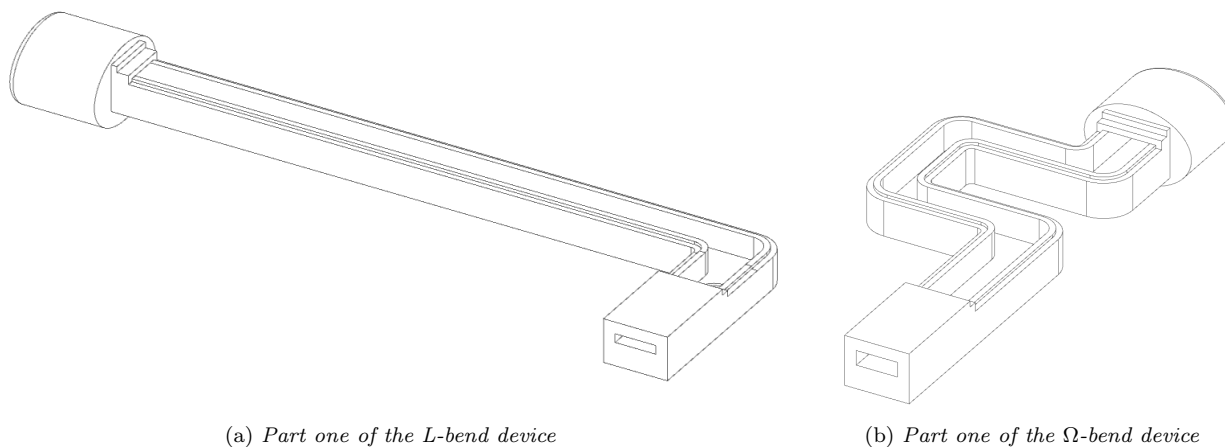


Figure 3.8: *Isomeric view of parts one of the devices used in the experimental testing.*

Part one is a hollow construction with walls. The inlet of the device can be seen closest to the viewer in Figure 3.8 as a rectangular cavity. The inlet is a closed construction with a roof. The exterior end part of the device, the outlet, is cylindrical in shape with rounded edges in order to adhere correctly and tightly to the silicone mouthpiece of the testing apparatus without damaging the silicone material. On top of the lateral walls, the second part of the devices is positioned. This part of the devices is the major roof: it covers a large portion of part one. Part two of the Ω -bend device can be seen in grey in Figure 3.9 positioned over part one.

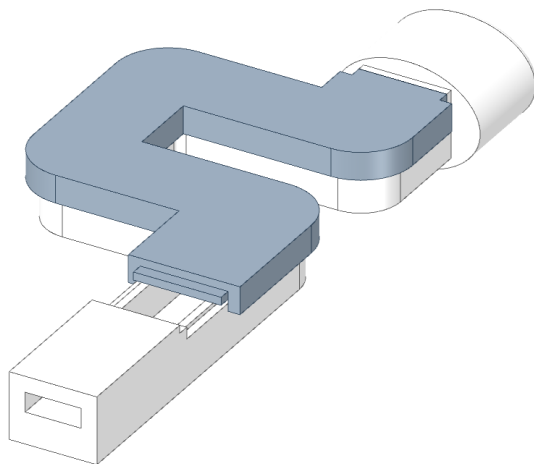


Figure 3.9: *Isometric view of part one, in white, and part two, in grey, of the Ω -bend device.*

To ensure that the different parts adhered tightly to each other, minimizing leakage that could affect the experimental results, part two has short lateral walls that cover the gaps that could be present between part one and part two. When part one and part two are connected, as can be seen in Figure 3.9, the whole geometry is covered except for an opening over the indentation, where the drug powder dose can be inserted from above. This opening can be closed with the last part, part three, which adheres tightly to rest of the device using the same design with lateral walls as part two. The fully assembled devices can be seen in Figure 3.10.

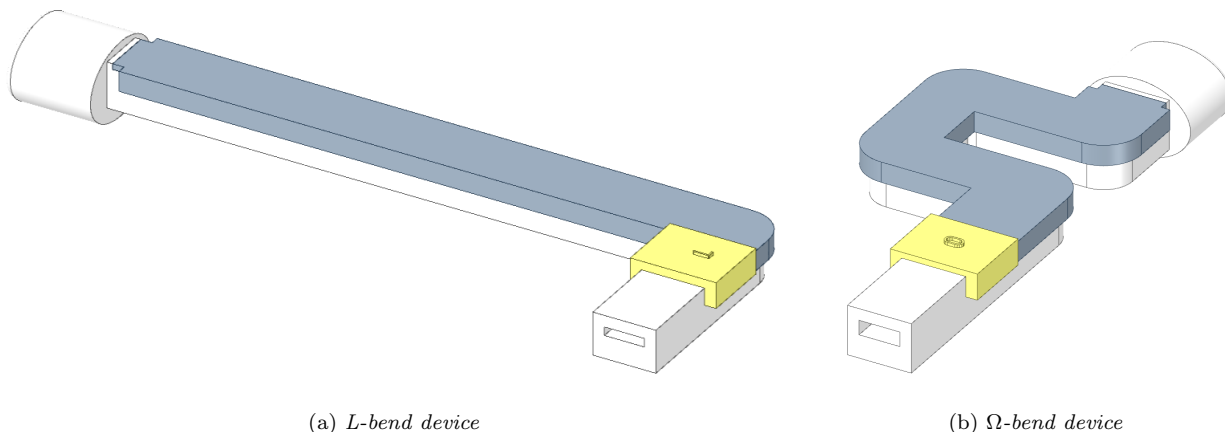


Figure 3.10: *Isometric views of the assembled devices used in the experimental testing. Parts one are white, parts two are grey and parts three are yellow.*

The L-bend device and the Ω -bend device were 3D-printed in three copies each. The 3D-printing process was an additive process, in which the construction material was added in layers. Wax was used as support material in order to 3D-print the hollow regions of part one: the inlet and the cylindrical outlet. The wax was

then melted and removed from the finished devices, but some residues were still present. The 3D-printing process generated some patterning with stripes on the surface of the devices depending on how the device was oriented in the 3D-printing machine. The internal surface of the devices is therefore not perfectly smooth and the surface roughness of part one is different between the copies of the same device, since some copies have stripes on the surface mainly along the flow direction and others have stripes orthogonal to the flow direction. The different kinds of patterning can be seen in Figure 3.11, and will from now on be denoted as horizontal patterning (H-pattern) and vertical patterning (V-pattern), referring to how the patterning is oriented when looking at the geometry from above.

As can be seen in Figure 3.11a and Figure 3.11b, the H-pattern is parallel to the flow direction in most of the L-bend device, while the V-pattern is mostly perpendicular to the flow direction. The same reasoning applies for the Ω -bend device in Figure 3.11c and Figure 3.11d.

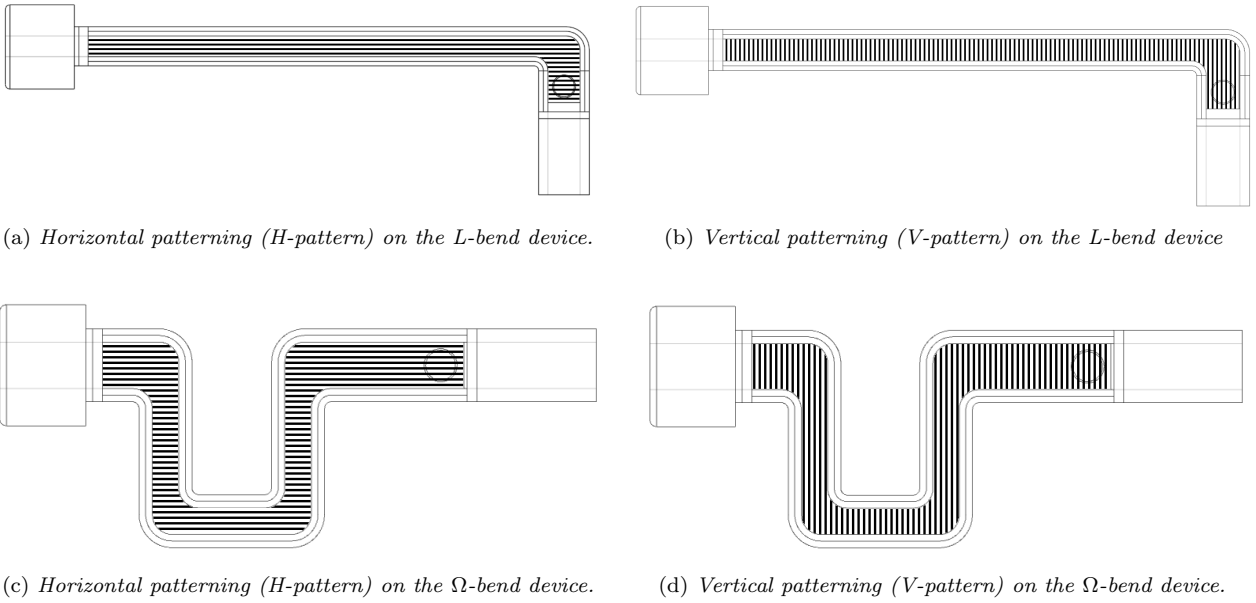


Figure 3.11: Top view of part one of the devices with two different kinds of patterning.

The previously mentioned differences in patterning for the copies of the L-bend devices and the Ω -bend devices are listed in Table 3.4.

Table 3.4: List of the orientation of the inner surface pattern of part one for the three copies of the devices.

Copy	L-bend			Ω -bend		
	L1	L2	L3	Ω 1	Ω 2	Ω 3
Patterning orientation	H	H	V	V	H	V

One more copy of the L-bend device and the Ω -bend device, respectively, were also 3D-printed. That gave a total of four copies for each geometry. The fourth copies were not used in the experimental testing to obtain data, but to visualize how the powder moved through the devices. As mentioned in section 3.1, visualization was also the reason for adding the backwards facing step. It was believed that the re-circulation region generated could slow down the powder from simply blowing straight out of the devices. In order further ease the visualization, the bottom of the fourth copies was coloured black and part two, which represents the majority of the roof, was sanded and treated with a clear coat to make it transparent. The fourth copy of the L-bend device can be seen in Figure 3.12.

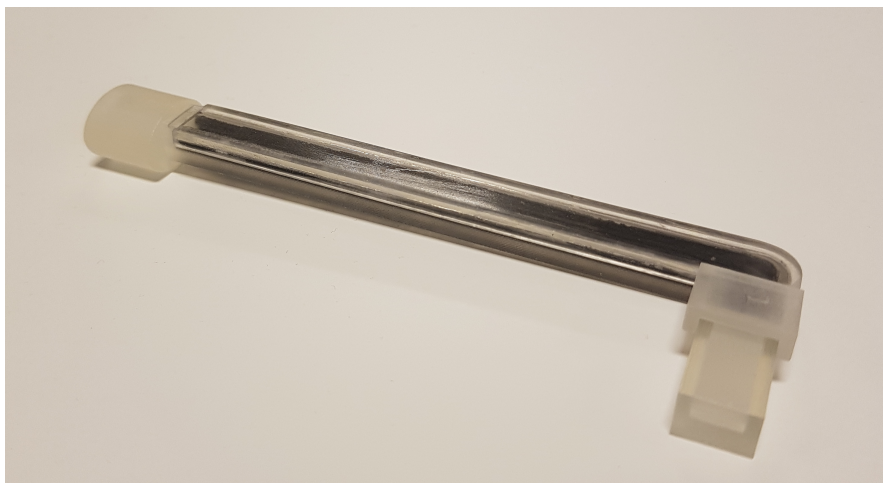


Figure 3.12: *The fourth copy of the L-bend device used for visualization.*

3.3.2 Experimental set-up, testing procedure and measurements

The powder used in the experimental testing was a formulation containing lactose carrier particles, 4 % of the Active Pharmaceutical Ingredient (API) beclomethasone dipropionate and 1 % magnesium stearate. The testing procedures were performed three times on each of all the 3D-printed device copies. The instrument used in the testing was an Aerodynamic Particle Sizer (APS) TSI-3321. The APS was connected to a United States Pharmacopeia (USP) throat. A picture of the experimental set-up can be seen in Figure 3.13. The cylindrical part of the devices was attached to the USP throat. When the instrumentation was activated, air was drawn from the inlet of the device, through the outlet, the USP throat and finally through the APS, with a flow rate reaching a maximum of 40 lpm in 1.5 s for the Ω -bend and in 1 s for the L-bend. The rise times of the flow in one empty L-bend device and one empty Ω -bend device were measured and found to be 240 ms and 195 ms, respectively.



Figure 3.13: *View of the experimental testing instrumentation. In the left upper corner, the USP throat to which the devices were attached can be seen. The USP throat is connected underneath to three pre-separators, as was used for the testings on the Ω -bend devices. The pre-separators are in turn connected to the APS, that can be seen in the lower part of the figure.*

The first step of the testing procedure was weighting the tested device. The device was then filled with a powder dose, closed and weighted again to find the weight of the drug dose. The cylindrical part of the device was fixed to the USP portal. In order to get similar rise times in the APS for the two devices, three pre-separators were

used for the Ω -bend devices and two for the L-bend devices. The instrument was then started with a terminal flow rate of 40 lpm and data was collected. The device was weighted again after the test to see how much powder was retained. As previously mentioned in this section, the procedure described above was performed three times for each of the six 3D-printed devices. The devices were cleaned in different ways between the runs. After the first run, they were washed with water, after the second run they were cleaned with compressed air.

The fourth copies of the L-bend and Ω -bend devices were used to visualize the flow of the powder. The experimental set-up was the same as described above, but no data was collected. A camera was installed on a tripod over the device. The camera had a capability of 20 frames per second.

The measurements performed and the data collected in the experiments are summarized here. From the initial weight of the drug dose, knowing the size ratios of carrier particles and fine particles in the powder formulation, the initial mass of fine particles in the device was calculated. The APS could measure the particles emitted from the device with an aerodynamic diameter below 5 μm , i.e. the emitted fine particles. More in detail, the APS measured the mass and the size distribution of the emitted fine particles. The aerodynamic diameter is defined as the diameter a particle would have if it had the same velocity, but with a density of 1000 kg/m^3 [12]. Another property obtained from the APS, was the Mass Median Aerodynamic Diameter (MMAD) of the emitted fine particles, which is the median of the distribution of the particle mass with respect to the aerodynamic diameter [13]. The aerodynamic diameter can be useful to characterizes particle deposition in human lungs and filtration [14]. It is therefore included in the study to make the results comparable with other experimental testings or papers, but is not analyzed any further since the tested devices are not meant to be representative of real inhalers in terms of these characteristics. Furthermore, by weighting the device after the testing, the mass of the retained drug dose was found. Finally also the pressure drop of the devices were measured during each test.

4 Results

In this chapter the results of this master's thesis are presented. First, the results of the numerical simulations are given, divided into an overview of central notions, general results, base case simulations and sensitivity analyses. The sensitivity analyses includes a study of the use of parcels, the sensitivity to the value of the surface energy and the values of the diffusion coefficient of the scalar transport equations. Second, the experimental results are presented. Finally the comparable results between the simulations and the experiments are highlighted.

4.1 Simulations

The results of the numerical simulations are presented in this section in the following order. First some central notions are defined for understanding the terminology of the results. Then general results common to all cases are highlighted, followed by the results of the base case simulations, L-base and Ω -base. Finally the results for the sensitivity analysis on the use parcels, surface energy and diffusion coefficients are presented.

4.1.1 Overview of central notions concerning the results

Before the results for the simulated cases are presented, an overview of some central notions and concepts is given. When analyzing the results for the carrier particles or parcels, the behaviour over time is an interesting property, together with the amount and location of retention of carrier particles in the geometry. Also the behaviour of emitted fine particles over time is analyzed and compared. For the carrier particles and parcels, the median number of collisions registered is presented, together with the number of collisions with walls or with other carrier particles or parcels. The averaged collision energy for particle-wall and particle-particle impacts are also given.

As mentioned in section 2.3.1, the micro-models describe the behaviour of fine particles. According to these micro-models four different outcomes can be identified for the fine particles. First, in all the three micro-models, a fraction of fine particles is detached from the carrier particles into the flow field and is thereafter emitted from the device. This outcome is referred to as Fraction of Fine particles Emitted (FFE) from now on. Second, upon a wall collision, a fraction can attach to the walls, referred to as FFW. Finally, some fine particles might not detach from the carrier particles. The fraction of fine particles attached to carrier particles retained in the geometry is referred to as FFCR, and the fraction of fine particles attached to carrier particles emitted from the geometry is called FFCE.

The importance of each mechanism in terms of detachment of fine particles can be quantified by looking at the percent of fine particles emitted by wall collisions, particle-particle collisions or drag dispersion. Finally, also the concentration of fine particles attached to the walls is presented.

4.1.2 Common results for the simulations

Some results are common for all the studied cases and are therefore presented in this section. All L-bend cases, except for L-Base, were simulated to 350 ms and all Ω -bend cases to 400 ms. The reason for this is that when the rise time for respective geometry is reached, most detached fine particles have left the domain and the carrier particles have adhered to the walls or have been emitted. After the rise time is reached, the flow velocity increases very slowly and only slightly, see Figure 3.7, which indicates that the results would not be affected considerably by running the simulations further. Also common to all simulations is that the residuals showed good convergence.

In the simulations, it was also found that drag dispersion only contributes to the detachment of fine particles with a maximum of 0.011 % of the fraction of emitted fine particles, which is rounded to 0 % hereafter, since only a precision of maximum two decimals is used. In all cases, when looking at the behaviour of carrier particles and fine particles, it was found that the carrier particles retained in the geometries have around 90 % of the initial fine particles still attached. Further, it was seen that the time profiles of carrier particles

and fine particles emitted from the geometries have a very similar behaviour. For all simulations the fine particles behaved in accordance with the observed dynamics of the carrier particles, which indicates that the implementation of the micro-models into the CFD software was adequate.

The fluid phase in all simulations has similar features and the carrier particles do not seem to influence the fluid phase considerably. The fluid phase of the L-bend, simulated without particles, can be seen in Figure 4.1. The figure shows the velocity streamlines of the fluid phase at four different time steps. At the beginning the inlet velocity is low, but it increases rapidly, as can be seen in Figure 3.7. The velocity of the fluid is high at the inner side of the bend and low on the outside of the bend.

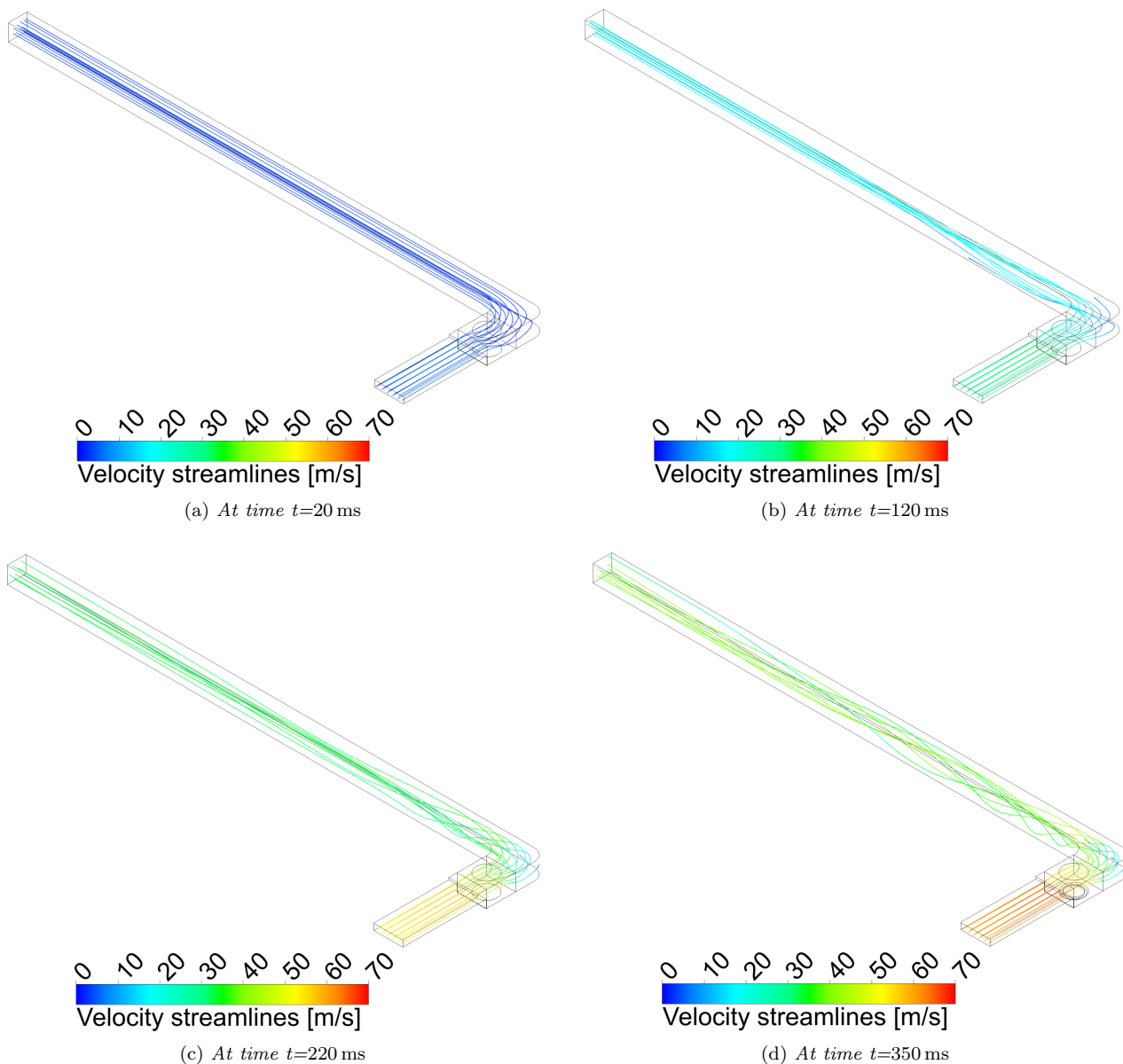


Figure 4.1: Velocity streamlines of the fluid phase in the L-bend simulated without particles. The figures are taken at four different flow times illustrating the fluid velocity shortly after the beginning of the simulation, at the end of the simulation and at two times in between.

As the inlet velocity increases, also a re-circulation region emerges and develops under the step. It can be seen clearly in the lateral views of Figure 4.2. The re-circulation region is quite large and reaches all the way behind the indentation. The inlet velocity is high for the later time steps and decreases close to the wall.

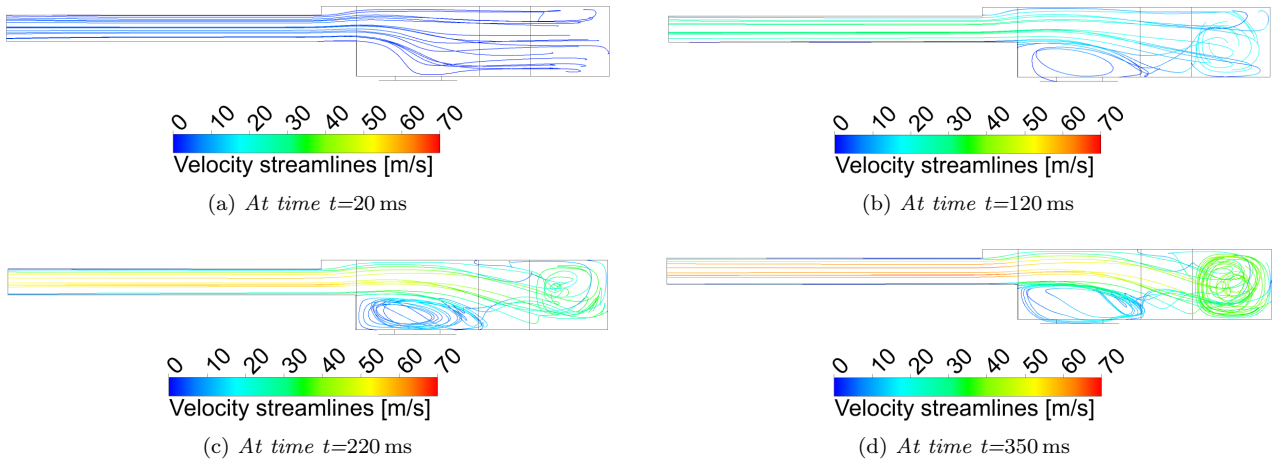


Figure 4.2: Lateral close-up of the velocity streamlines in Figure 4.1 of the fluid in the re-circulation region for the L-bend. The inlet is located on the left side of the figures.

The fluid phase in the Ω -bend shows features similar to the L-bend. In Figure 4.3 the velocity streamlines for the Ω -bend simulated without particles can be seen. The velocity is generally lower in all shown time steps compared to the L-bend, as the inlet velocity is lower (see Figure 3.7).

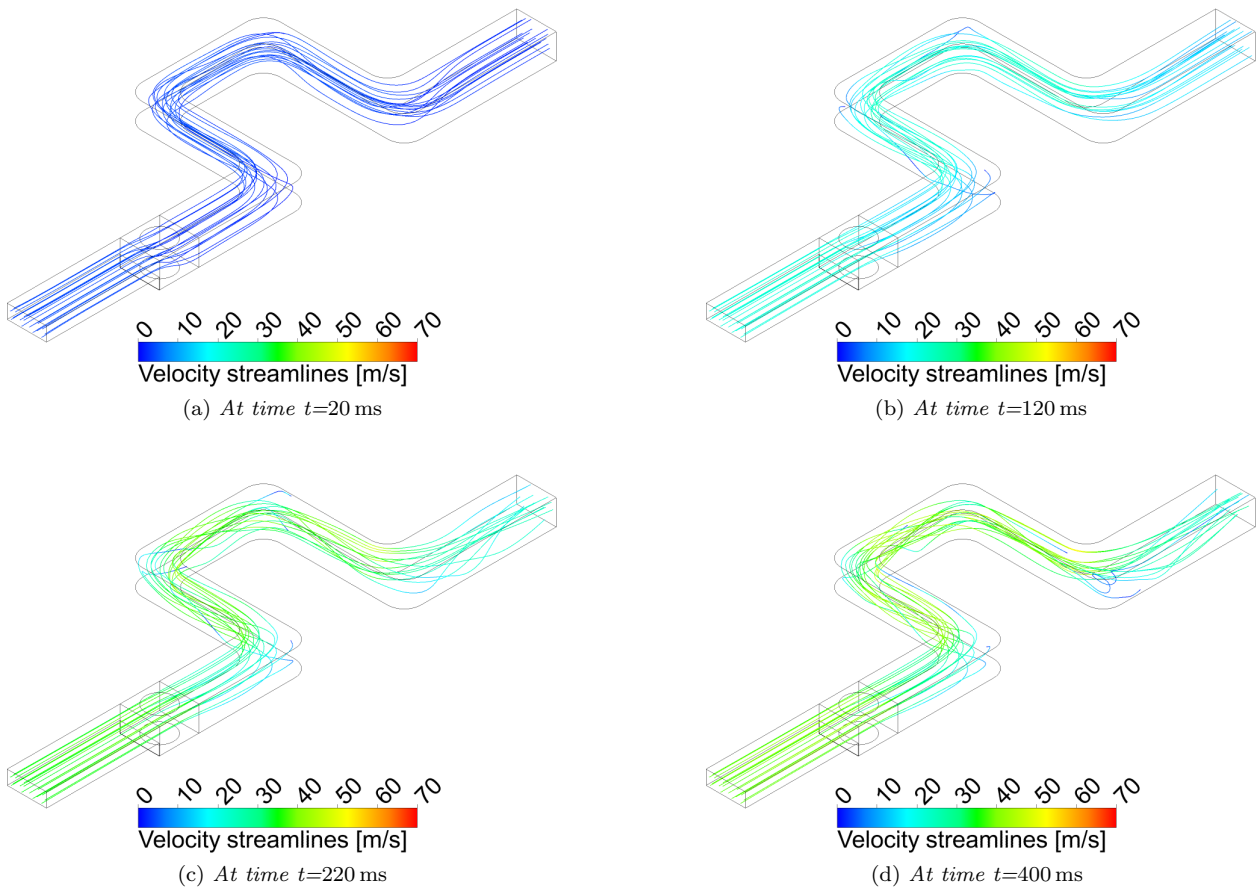


Figure 4.3: Velocity streamlines of the fluid phase in the Ω -bend simulated without particles. The figures are taken at four different flow times illustrating the fluid velocity shortly after the beginning of the simulation, at the end of the simulation and at two times in between.

Also the re-circulation region for the Ω -bend, which can be seen in Figure 4.4, has very similar features to the re-circulation region for the L-bend.

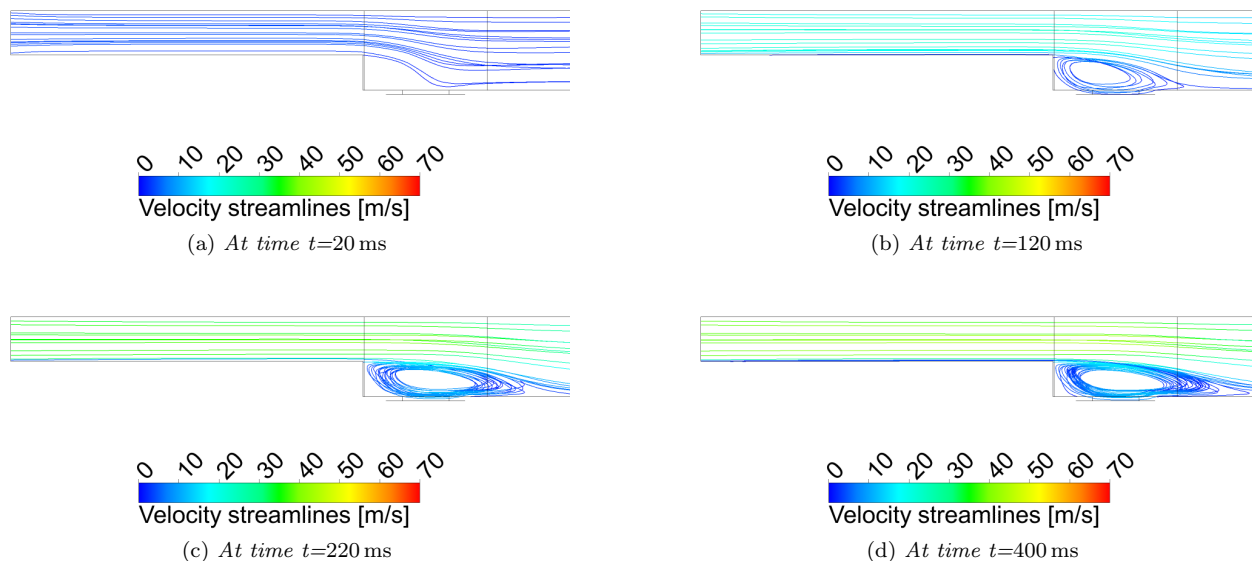


Figure 4.4: Lateral close-up of the velocity streamlines in Figure 4.3 of the fluid in the re-circulation region for the Ω -bend. The inlet is located on the left side of the figures.

The pressure drop obtained when simulating the L-bend without particles at 350 ms is 2.6 kPa. At this time step, the fluid has not yet reached its maximum inlet velocity even if it is very similar to it. The fluid phase was therefore also simulated until 500 ms, the time at which the pressure drop stabilized to a value of 3.0 kPa. For the Ω -bend the pressure drop is 2.0 kPa at 400 ms.

4.1.3 Base case simulations

The base case simulations were run to be able to compare the results of the numerical simulations with the results from the experimental testing for both geometries. Further, the results for the two base cases are also compared to evaluate the different geometries. Both cases were initially injected with 25 000 particles, grouped in 2500 parcels to save computational power. The results are presented below, first for the case L-Base and thereafter for the case Ω -Base.

L-Base

The simulation L-Base was run until a flow time of 211 ms. At that time, the simulation was terminated since all carrier particles and all detached fine particles had left the geometry. The behaviour of the carrier particles, which were simulated using parcels, are shown in Figure 4.5. The parcels were initialized at the indentation and stayed there until a flow time of 65 ms, when the velocity of the fluid was large enough to start accelerating the parcels. During this time, there were no collisions, and therefore the drag force acting on the carrier particles was the only contribution to the detachment of fine particles. At 65 ms, some parcels started to move away from the indentation. They followed the re-circulated flow and moved backward and up toward the inlet. Thereafter, they were accelerated by the flow until they collided with the wall at the bend. The first parcel collided at the bend at a flow time of around 80 ms, which can be seen in Figure 4.5a. At a flow time of 98 ms, the first parcel left the geometry. Thereafter, a steady flow of parcels re-circulated backward and upwards, following the fluid flow and left the geometry. After 140 ms, the steady flow of parcels started to dilute. The last parcel left the indentation at around 200 ms. Finally, the last parcel had left the geometry at 211 ms, which is before

the velocity of the fluid have reached its maximum. Hence, there was no retention of carrier particles for the L-Base case.

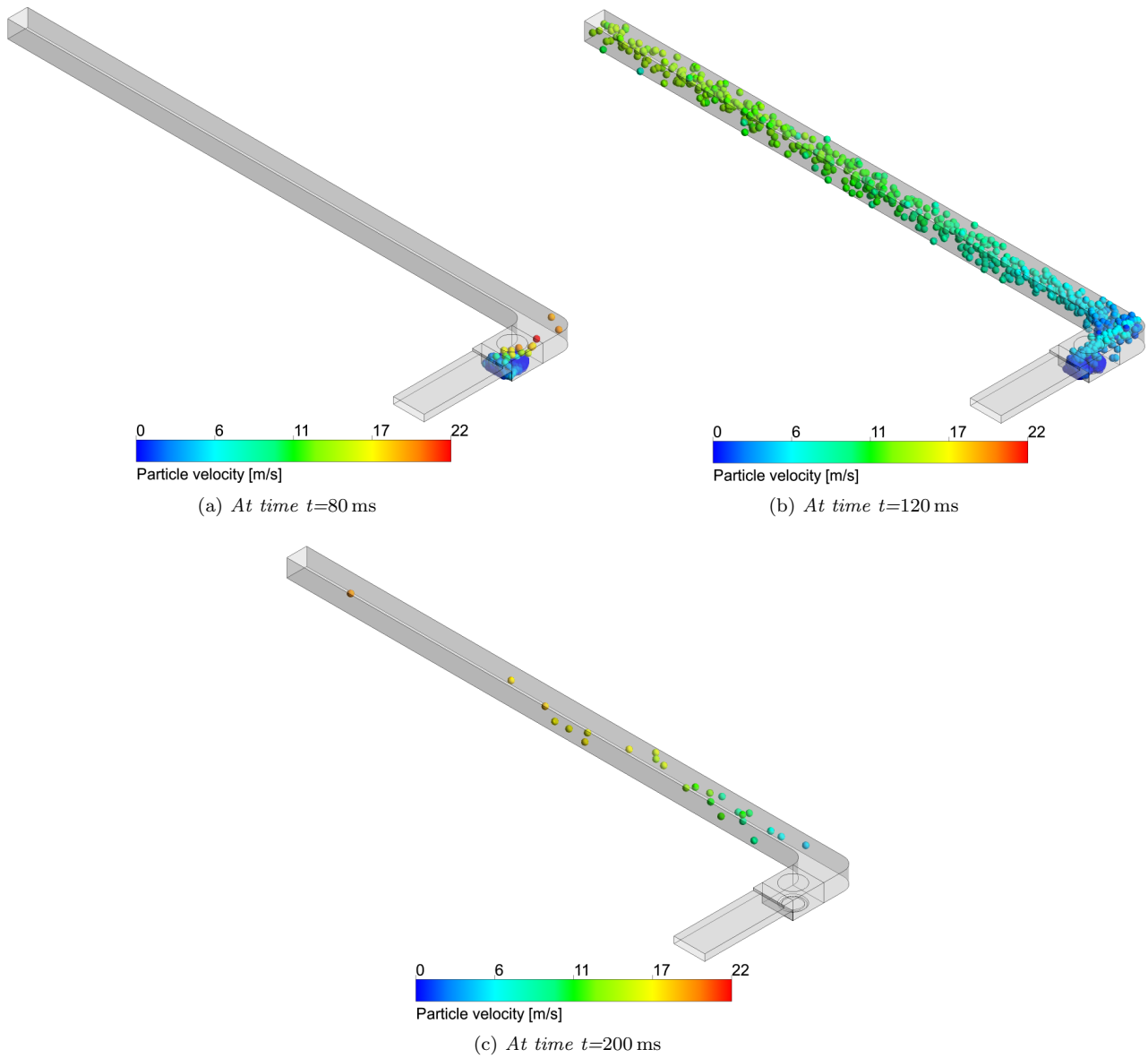


Figure 4.5: *Position and velocity of carrier particles grouped in parcels at four different times illustrating a) the first particle-wall collisions at the bend, b) the steady flow of parcels and c) the final parcels leaving the geometry.*

Figure 4.6 shows the cumulative number of carrier particles emitted from the geometry over time in blue, with the y-axis to the left and fine particles emitted over time in green, with the y-axis to the right. It should be noted that the scale of the two axis is different. It can be seen that time profiles of the carrier particles and the fine particles leaving the geometry are very similar for the two different type of particles: both the carrier particles and the fine particles were emitted from the geometry between around 100 ms and 200 ms after the start of the simulations.

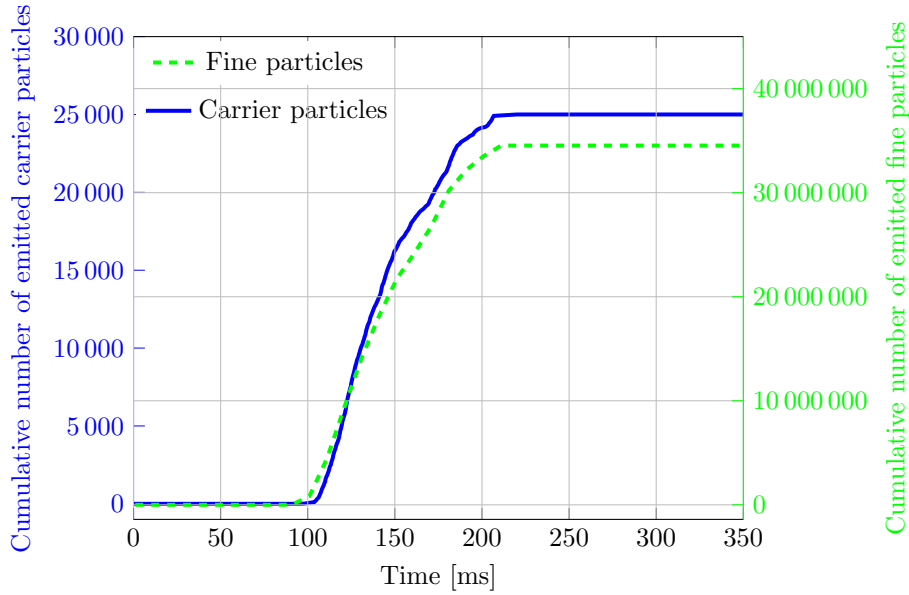


Figure 4.6: Cumulative number of particles emitted from the geometry for the case L-Base. The blue axis on the left shows the number of carrier particles while the green axis to the right shows to number of fine particles.

The outcome of the fine particles at a flow time of 211 ms is illustrated in Figure 4.7. The majority of the fine particles were detached and emitted with the flow, see FFE. A minor part of the fine particles were attached to the walls due to particle-wall collisions, see FFW. Since there was no retention of carrier particles for the case L-Base, there was no fraction of fine particles attached to carrier particles retained in the geometry, see FFCR. FFCE shows that some fine particles were still attached to the carrier particles as they emitted the geometry.

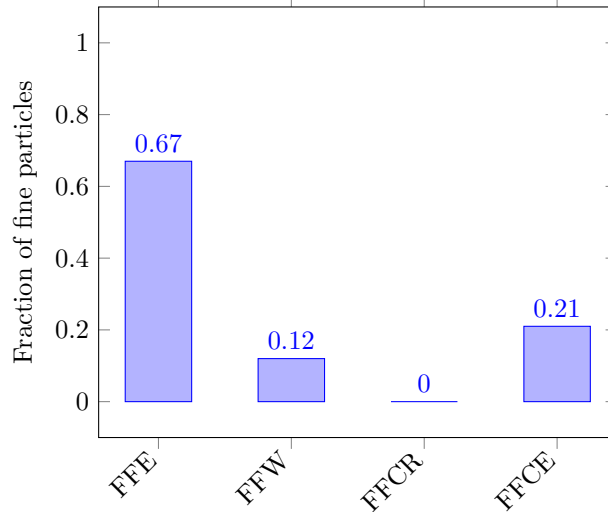


Figure 4.7: The outcome of fine particles for the case L-Base at time $t=211$ ms. FFE is the fraction of emitted fine particles, FFW the fraction of fine particles attached to wall, FFCR and FFCE the fraction of fine particles attached to retained carrier particles and emitted carrier particles, respectively.

To further investigate the detachment of fine particles, the fraction of fine particles released due to each mechanism was tracked. As previously mentioned, the drag force acting on the carrier particles was the only mechanism acting during the first 65 ms. As the carrier particles started to move, and with that collide, the other two mechanisms become much more important. At a flow time of 211 ms, 99.8 % of the number of fine particles had been released due to particle-wall collisions. This is therefore the most important mechanism for

detachment of fine particles for the L-Base case. 0.2 % of the fine particles were detached due to particle-particle collisions. Summarizing at the end of the simulations, the number of fine particles released due to drag force acting on the carrier particles is 0 %.

The number of collisions for all parcels with carrier particles was also investigated. The results for L-Base can be seen in Table 4.1. For the L-Base case, the median number of collisions is 24. This includes both particle-particle and particle-wall collisions. It can be seen that the parcels collide against the walls twice as often as they collide against other parcels. However, the average collision energy is more than three order of magnitudes larger for the particle-wall collisions. Hence, in average the parcels have a larger impact velocity when they collide with the walls of the geometry, compared to when they collide with other parcels.

Table 4.1: Summary of results in terms of collisions and collision energy for L-Base.

	L-Base
Median number of collisions per carrier particle	24
Number of particle-wall collisions	232 560
Number of particle-particle collisions	548 490
Average particle-wall collision energy [J]	5.5×10^{-10}
Average particle-particle collision energy [J]	1.5×10^{-13}

Figure 4.8 illustrates where the fine particles attached to the walls of the geometry upon particle-wall collisions. The concentration is defined as number of fine particles per unit area. It can be seen that the largest concentrations of fine particles are found at the walls of the indentation closest to the inlet and at the walls of the bend, see Figure 4.8b. The high concentration of fine particles close to the indentation is caused by many collisions with a small impact velocity. The impact velocity at collision with the walls of the bend is higher and that is when most of the fine particles attached to the carrier particles are detached into the air.

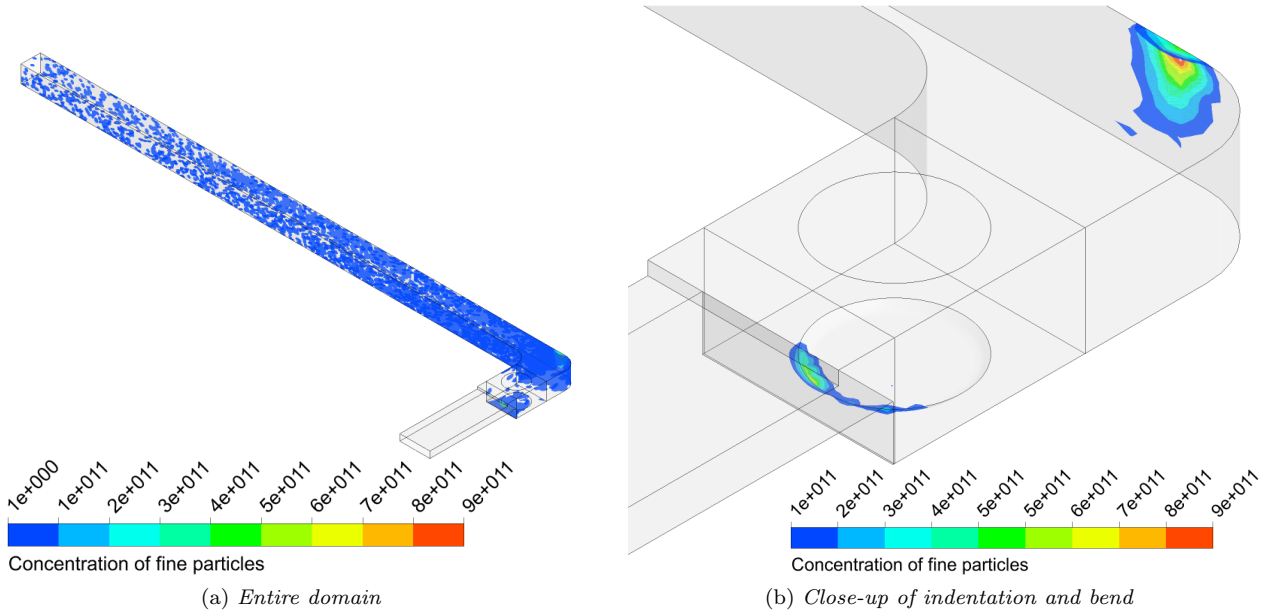


Figure 4.8: Concentration of fine particles attached to the walls for $t=211$ ms for the case L-Base. The concentration is defined as number of fine particles per unit area.

Ω -Base

The case Ω -Base was run until the carrier particles, grouped in parcels, had reached a state where no more parcels are assumed to leave the geometry. This corresponds to a flow time of 400 ms. To illustrate the behaviour of the carrier particles, Figure 4.5 shows the position and velocity of the parcels at four different flow

times.

The parcels started to leave the indentation after 75 ms. As can be seen in Figure 4.9a, the first parcels left the indentation moving backward and up toward the inlet. Thereafter they were accelerated by the flow and the first parcel reached the first bend after 90 ms. The first parcel left the geometry after 120 ms, see Figure 4.9b. The flow of parcels was steady until 160 ms, when it started to dilute. Finally, the last parcel left the geometry at a flow time of 220 ms. After this time parcels still in the geometry had zero velocity. In total 11 % of the initial number of carrier particles were retained. They were located close to the indentation, at the backward facing step, see Figure 4.9d.

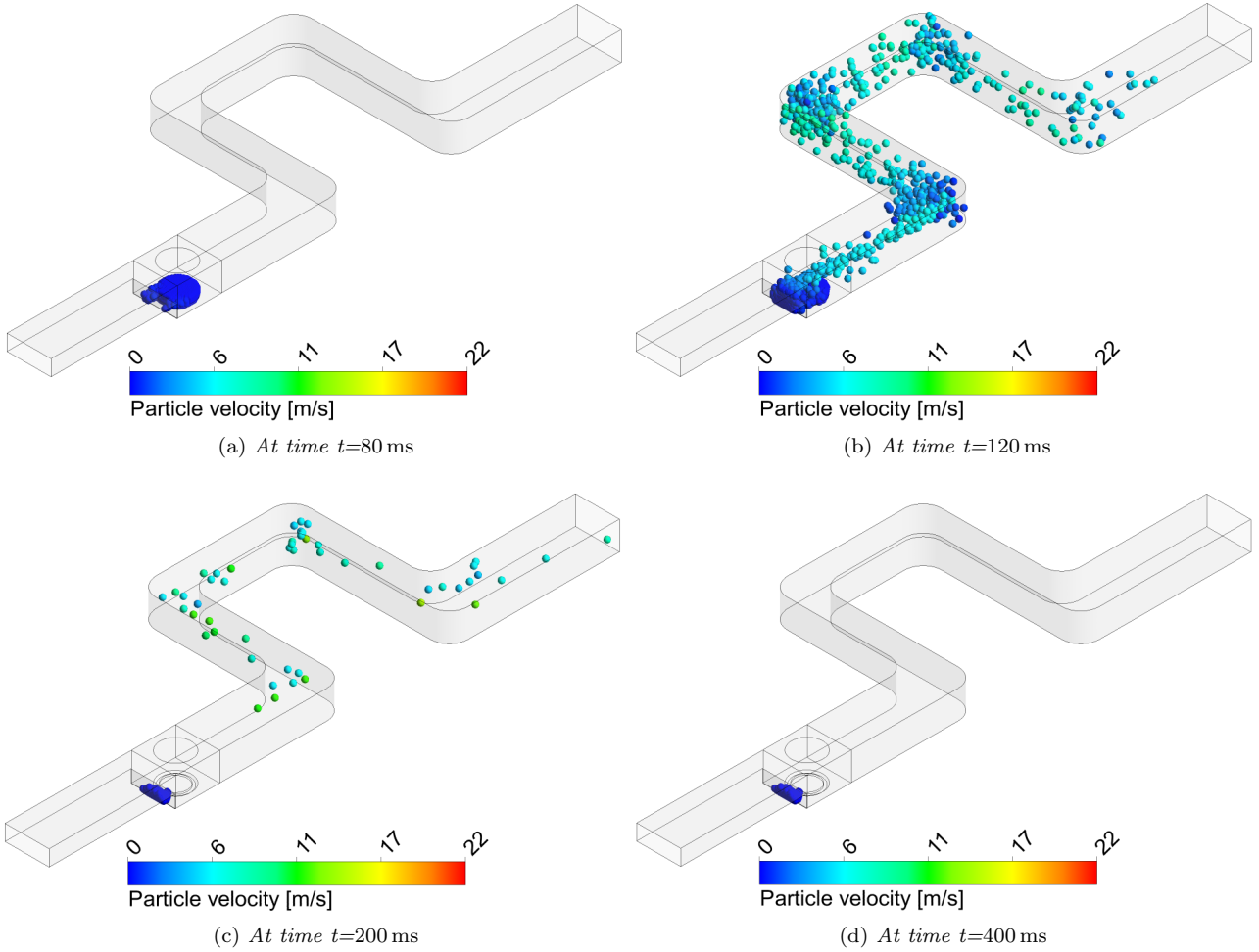


Figure 4.9: *Position and velocity of the carrier particles grouped in parcels at four different times, illustrating a) the first parcels leaving the indentation, b) the steady flow of parcels, c) the last parcels to leave the indentation and d) the retention of the parcels with carrier particles after 400 ms.*

The cumulative number of carrier particles and fine particles emitted over time can be seen in Figure 4.10. It should be noted that the y-axis are different for the two time profiles: the blue axis to the left shows the cumulative number of carrier particles and the green axis to the right shows the cumulative number of fine particles. It can be seen that the two time profiles are similar, even though the fine particles started to leave the geometry a bit earlier than the carrier particles.

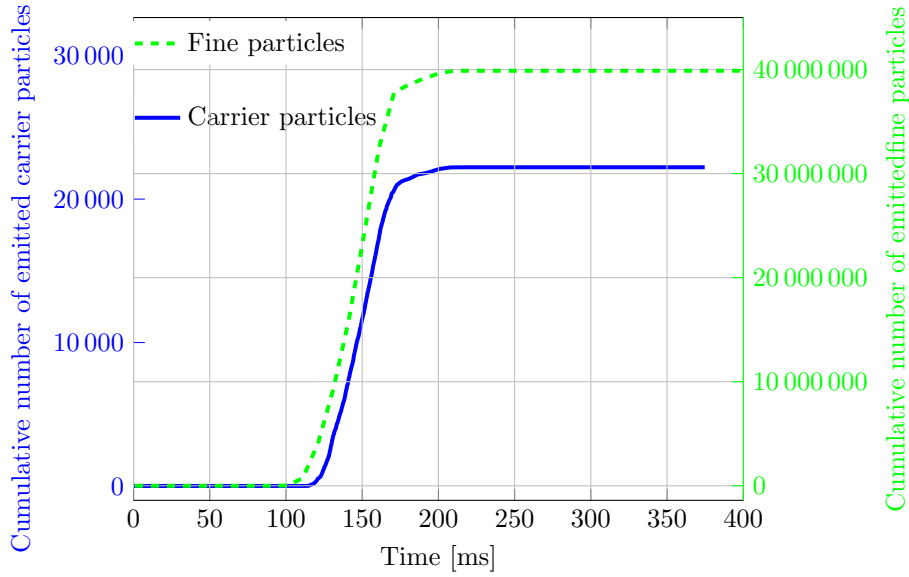


Figure 4.10: Cumulative number of particles emitted from the geometry for the case Ω -Base. The blue axis on the left shows the number of carrier particles, while the green axis to the right shows to number of fine particles.

The outcome of the fine particles at a flow time of 400 ms is shown in Figure 4.11. It can be seen that the majority of the fine particles was detached into the air, see FFE. Of the remaining parts, half was attached to the walls, see FFW, and the other half was attached to carrier particles still retained in the geometry, see FFCE. Hence, as desired for the Ω -bend geometry, there were no fine particles attached to the carrier particles which left the domain, see FFCE.

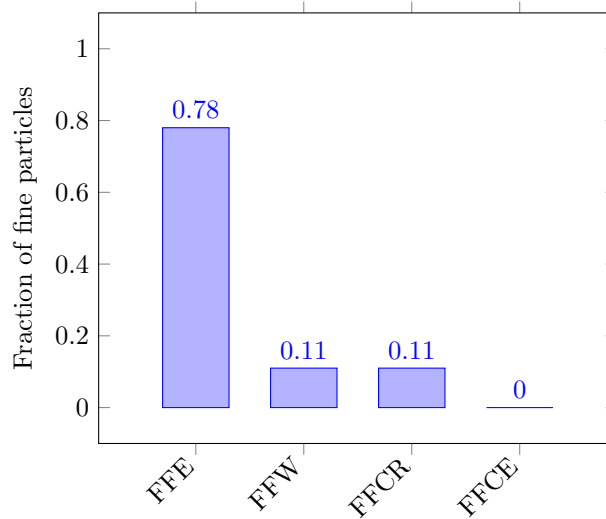


Figure 4.11: The outcome of fine particles for the case Ω -Base at time $t=400$ ms. FFE is the fraction of emitted fine particles, FFW the fraction of fine particles attached to wall, FFCE and FFCE the fraction of fine particles attached to retained carrier particles and emitted carrier particles, respectively.

Summarizing over the simulated flow time, 99.7 % of the fine particles were detached due to particle-wall collisions. The remaining 0.3 % was due to particle-particle collisions. The number of collisions can be seen in Table 4.2. It can be seen that the number of particle-particle collisions is almost two times the number of particle-wall collisions. However, the average collision energy was a bit over three orders of magnitude higher for the particle-wall collisions. Hence, the impact velocity was much higher for the particle-wall collisions.

Table 4.2: Summary of results in terms of collisions and collision energy for Ω -Base.

	Ω -Base
Median number of collisions per carrier particle	46
Number of particle-wall collisions	441 730
Number of particle-particle collisions	842 540
Average particle-wall collision energy [J]	2.2×10^{-9}
Average particle-particle collision energy [J]	7.7×10^{-13}

The concentration of fine particles attached to the walls can be seen in Figure 4.12. The concentration is defined as number of fine particles per unit area, and it is found to be the highest at the indentation and the bends, especially the first bend. A close-up of the two zones with the highest concentrations can be seen in Figure 4.12b. The high concentration of fine particles close to the indentation is caused by many collisions with a small impact velocity. The impact velocity at collisions with the walls of the bends is higher and that is when most of the fine particles detach from the the carrier particles.

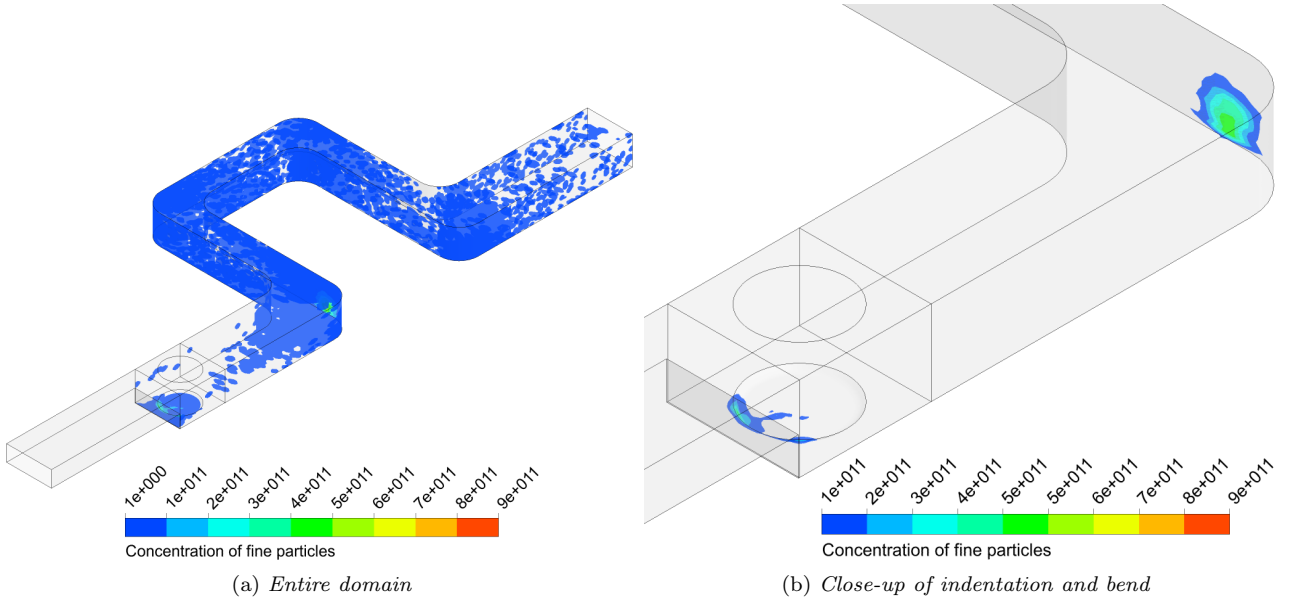


Figure 4.12: Concentration of fine particles attached to the walls for $t=400$ ms for the case Ω -Base. The concentration is defined as number of fine particles per unit area.

Comparison of L-Base and Ω -Base

The two geometries were designed to yield different results in terms of fraction of emitted fine particles. Comparing Figures 4.7 and 4.11 it can be concluded that a difference is achieved for the fraction of fine particles emitted (FFE): It was found to be 78 % for the Ω -Base and 67 % for L-Base, which give a difference of 11 percentage points. Also a difference was found for the fraction of fine particles which were still attached to the carrier particles as they were emitted from the geometry (FFCE): 0 % for Ω -Base and 21 % for L-Base. The fraction of fine particles attached to the walls (FFW) were almost the same for the two cases (11 % and 12 %, respectively). Also, the amount of retention of carrier particles differed between the two cases: there was no retention for L-Base, while 11 % of the carrier particles did not leave the geometry for Ω -Base. Further, the carrier particles reached a higher velocity in the L-bend and left the geometry earlier for L-Base compared to Ω -Base, see Figures 4.5 and 4.9.

Comparing the time profile for carrier particles and fine particles emitted from the geometry, see Figures 4.6 and 4.10, it can be seen that the profiles for the fine particles are very similar for the two base cases. The fine particles are emitted between 100 ms and around 200 ms. The same time profile can be seen for the carrier

particles in the L-Base case. However, for the case Ω -Base the carrier particles start to leave the geometry later due to the lower flow rate, after around 130 ms.

The number of collisions is higher for the carrier particles in Ω -Base, both the median number of collisions per carrier particle and in total for particle-particle collisions and particle-wall collisions. This was aimed for in the design of the two geometries by including more bends for the Ω -bend, see section 3.1. However, the ratio between particle-particle and particle-wall collisions were similar for the two geometries. The number of particle-wall collisions was found to be 52 % of the number of particle-particle collisions for the Ω -bend. Corresponding value for the L-bend was 42 %. In both base cases, particle-wall collisions are the most important detachment mechanism for the release of fine particles. More than 99 % of the fine particles were released due to this type of collision. The average collision energy was larger for the Ω -Base case. For particle-wall collisions it was found to be 4 times larger. Corresponding number for the particle-particle collision was found to be 5 times larger. The concentration of fine particles attached to the walls showed the same trends for the two cases: high concentrations of fine particles attached to the walls was found close to the indentation and the bends. For both cases, the high concentration of fine particles at the indentation was caused by many wall collisions with a low impact velocity. The impact velocity for particle-wall collisions at the bend of the L-bend and bends of the Ω -bend was higher.

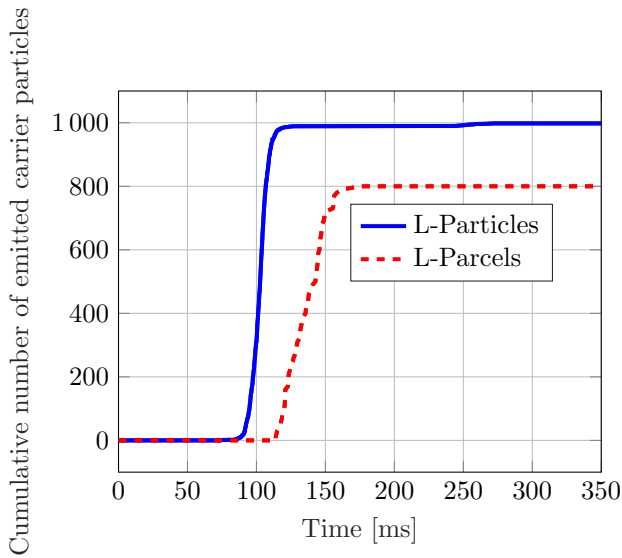
4.1.4 Sensitivity analysis of the use of parcels

In the sensitivity analysis of the use of parcels, it is important to compare the results for the simulations with individual carrier particles and the simulations with carrier particles grouped in parcels. This is done for both the L-bend and the Ω -bend by simulating 1000 carrier particles and 100 parcels, each parcel containing 10 carrier particles. To ensure that a good statistical sample is achieved when simulating 2500 parcels in the base case simulations and in the other sensitivity analyses, the use of parcels is also evaluated for 10 000 carrier particles. This is done for the L-bend in the L-Particles2 and L-Parcels2 cases. If, by increasing the number of carrier particles simulated, the results for the cases with individual carrier particles and the cases with parcels prove to be more similar, the results of the simulations with 2500 parcels can be considered to be representative of the behaviour of individual carrier particles. Below the results of the sensitivity analysis are presented first for the L-bend and then for the Ω -bend.

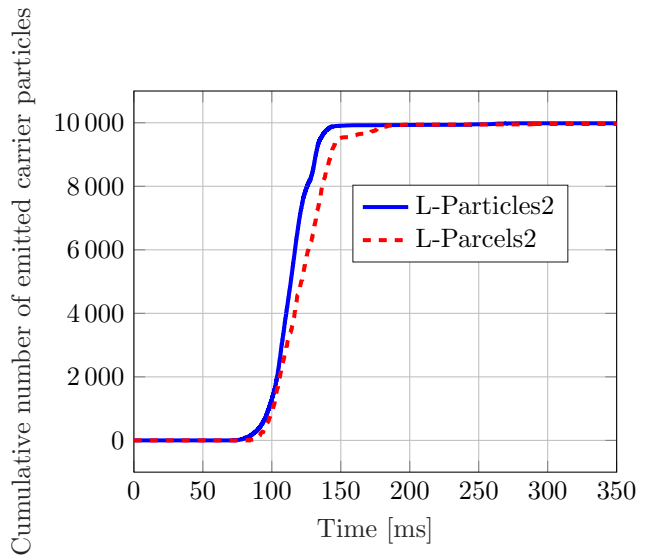
L-bend cases

The first sensitivity analysis performed was the simulations of the L-Particles and the L-Parcels cases, with 1000 carrier particles and 100 parcels, each containing 10 carrier particles, respectively. To ensure that a good statistical sample is achieved, this sensitivity analysis was also performed with a larger number of carrier particles in the simulations L-Particles2 and L-Parcels2. In these simulations 10 000 carrier particles were used and 1000 parcels each containing 10 carrier particles, respectively. Therefore, the presentation of these results focuses on the comparison between L-Particles and L-Parcels, and between L-Particles2 and L-Parcels2.

To begin with, the results differ in terms of retention of carrier particles in the geometry between the L-Particles and the L-Parcels simulations. Only one carrier particle was retained at the step for L-Particles, while in L-Parcels 19 parcels, corresponding to 190 carrier particles, are attached to the same region. For the simulations with 10 000 carrier particles, the results are more similar: 15 carrier particles were retained for L-Particles2 and 30 for L-Parcels2, which corresponds to 0.15 % and 0.3 %, respectively, of the initial amount of carrier particles. In order to give an understanding of the behaviour of particles and parcels with particles, the time profile of carrier particles emitted from the device can be seen in Figure 4.13. It can be seen that the carrier particles in the L-Particles simulation leave the geometry approximately 50 ms earlier than the parcels in the L-Parcels simulation. The parcels are also retained in the geometry to a larger extent. In Figure 4.13b it can be seen that the behaviour of carrier particles and parcels is much more similar when increasing the number of carrier particles simulated.



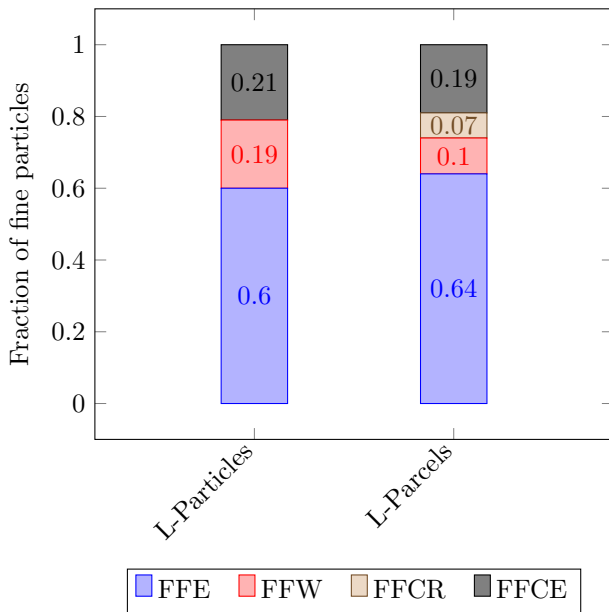
(a) *L-Particles* and *L-Parcels*.



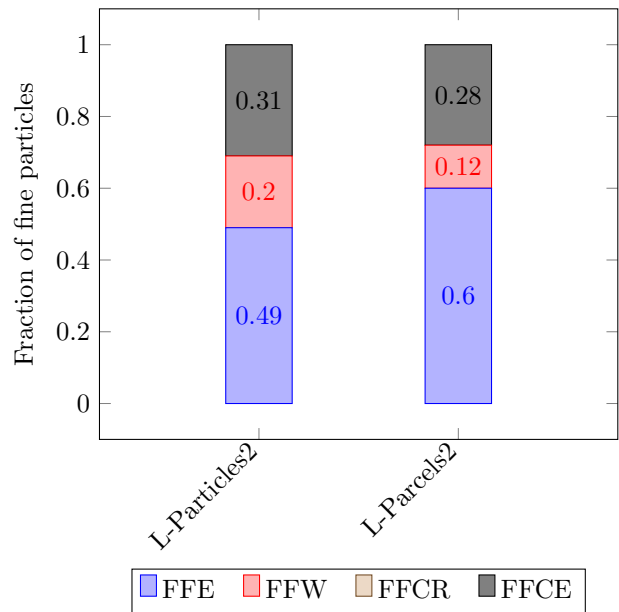
(b) *L-Particles2* and *L-Parcels2*.

Figure 4.13: Cumulative number of carrier particles emitted from the geometry over time for the sensitivity analysis on the use of parcels in the L-bend. *L-Particles* was injected with 1000 carrier particles, *L-Parcels* with 100 parcels, *L-Particles2* with 10000 carrier particles and *L-Parcels 2* with 1000 parcels.

Another property that can be compared is the outcome of fine particles. In Figure 4.14a and Figure 4.14b, the fraction of fine particles emitted, attached to walls, to retained carrier particles and to emitted carrier particles can be seen for the cases corresponding to 1000 carrier particles and 10000 carrier particles respectively.



(a) 1000 carrier particles and 100 parcels, respectively.



(b) 10000 carrier particles and 1000 parcels, respectively.

Figure 4.14: The outcome of fine particles for the cases a) *L-Particles* and *L-Parcels*, b) *L-Particles2* and *L-Parcels2* at time $t=350$ ms. Each parcel contains 10 carrier particles. *FFE* is the fraction of emitted fine particles, *FFW* the fraction of fine particles attached to wall, *FFCR* and *FFCE* the fraction of fine particles attached to retained carrier particles and emitted carrier particles, respectively.

The amount of carrier particles retained affects the results for L-Particles and L-Parcels, as seen in Figure 4.14a. Since no carrier particles stay in the geometry for the L-Particles case, FFCR is zero. The fraction of fine particles attached to the walls, FFW, is larger in L-Particles and the fraction of emitted fine particles, FFE, is similar in the two simulations.

As can be seen in Figure 4.14b, for both the simulations with more carrier particles, L-Particles2 and L-Parcels2, FFCR is negligible. Similarly to what was seen in Figure 4.14a, also Figure 4.14b shows that slightly more fine particles attached to the walls and less fine particles were emitted for the case with individual carrier particles L-Particles2 compared to the case with parcels L-Parcels2.

Of the fine particles emitted from the geometry, for L-Particles it is found that 98.2 % have been detached due to wall collisions and 1.8 % by particle-particle collisions. For L-Parcels the same percent ratios are 99.98 % and 0.02 %, respectively. This indicates that the use of parcels slightly underestimates the importance of particle-particle collisions and that wall collisions are the dominant mechanism for detachment of fine particles. For the simulations with 10 000 carrier particles, L-Particles2, similar results are found: 95.3 % of emitted fine particles were detached by wall collisions and 4.7 % by particle-particle collisions. For the L-Parcels2 simulations these values are 99.91 % and 0.09 % respectively.

In Table 4.3 the results for the number of collisions and the collision energy for the four cases are presented. It can be seen that the use of parcels underestimates the number of collisions. The mean particle-particle collision energy is one to two magnitudes lower when using parcels. However, the mean particle-wall collision energy has the same magnitude for all cases. The increase of particle-particle collisions compared to wall-particle, when increasing the number of carrier particles simulated, is also captured using parcels.

Table 4.3: Summary of results in terms of collisions and collision energy for the sensitivity analysis on the use of parcels in the L-bend.

	L-Particles	L-Parcels	L-Particles2	L-Parcels2
Median number of collisions per carrier particle	24	16	35	18
Number of particle-wall collisions	15 690	7470	181 360	71 130
Number of particle-particle collisions	10 030	6950	205 460	116 280
Average particle-wall collision energy [J]	1.5×10^{-10}	5.5×10^{-10}	1.3×10^{-10}	4.1×10^{-10}
Average particle-particle collision energy [J]	6.2×10^{-12}	4.4×10^{-14}	5.7×10^{-12}	1.1×10^{-13}

The concentration of fine particles on the walls is also compared between the four studied cases. All cases present the highest concentration of fine particles attached to the walls in the same regions as the L-Base and the Ω -Base cases (see section 4.1.3). Compared to the simulations with individual particles, the corresponding simulations with parcels have a more dilute concentration of fine particles.

Based on the results presented in this section, grouping 10 carrier particles in a parcel is considered to be representative of the behaviour of the individual carrier particles. Especially since the behaviour of carrier particles is captured better when increasing the statistical sample. Thus, this approach is found to be satisfactory for the simulations using 2500 parcels with 25 000 carrier particles, which are used in the base cases and the other sensitivity analyses mentioned in Table 3.2 and Table 3.3.

Ω -bend cases

As for the L-Particles and the L-Parcels simulations, also Ω -Particles and Ω -Parcels were simulated with 1000 particles and 100 parcels, respectively. The number of carrier particles retained for the two cases is 188 individual particles and 12 parcels. This corresponds to 19 % and 12 % of the initial number of carrier particles, respectively. The emitted carrier particles over time can be seen in Figure 4.15. Compared to L-Particles and L-Parcels it can be seen in Figure 4.13a that the carrier particles and the parcels behave more similarly in the Ω -bend. A difference however is that the parcels leave the geometry in several rounds, while the outflow of carrier particles is more continuous in Ω -Particles.

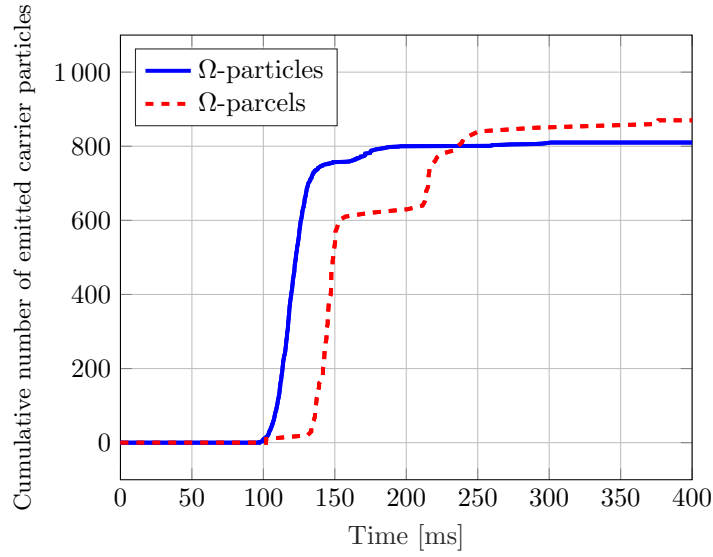


Figure 4.15: Cumulative number of carrier particles emitted from the geometry over time for the Ω -Particles (1000 carrier particles) and the Ω -Parcels (100 parcels) simulations.

In Figure 4.16, it can be seen that when using parcels the fraction of emitted fine particles (FFE) is larger and the fraction of fine particles attached to the walls (FFW) is minor, compared to when using individual particles. This was also found to be the case for the L-bend in Figure 4.14. FFCR is very similar between Ω -Particles and Ω -Parcels. FFCE is zero for both, since the carrier particles and parcels emitted have collided considerably, leaving no fine particles attached to the carrier particles as they were emitted from the geometry.

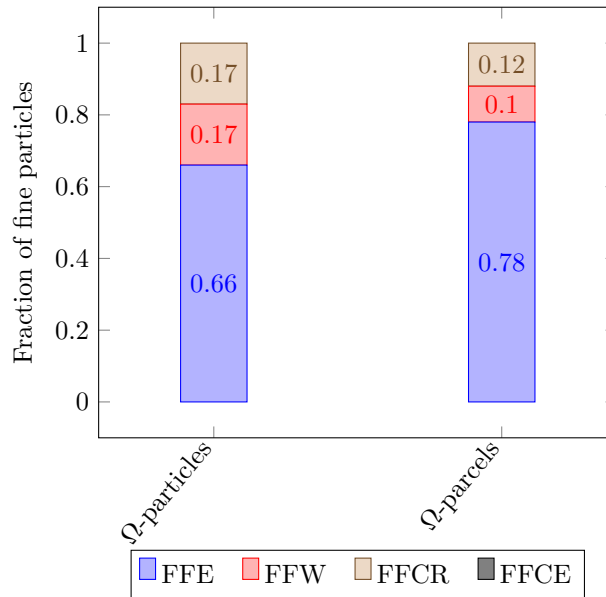


Figure 4.16: The outcome of fine particles for the cases Ω -Particles (1000 carrier particles) and Ω -Parcels (100 parcels) at time $t=400$ ms. FFE is the fraction of emitted fine particles, FFW the fraction of fine particles attached to wall, FFCR and FFCE the fraction of fine particles attached to retained carrier particles and emitted carrier particles respectively.

The mechanisms for detachment of fine particles proved to have the same importance as seen for the sensitivity analysis on the use of parcels for the L-bend: wall-collision were clearly dominant with 98.5 % of emitted fine particles for Ω -Particles and 99.9 % for Ω -Parcels. Particle-particle collisions were minor with 1.5 % and 0.02

% of emitted fine particles respectively. In Table 4.4, the results in terms of amount of collisions and collision energy for the two cases Ω -Particles and Ω -Parcels can be seen.

Table 4.4: Summary of results in terms of collisions and collision energy for the sensitivity analysis on the use of parcels in the Ω -bend.

	Ω -Particles	Ω -Parcels
Median number of collisions per carrier particle	40	25
Number of particle-wall collisions	26 960	16 450
Number of particle-particle collisions	15 100	8560
Average particle-wall collision energy [J]	8.6×10^{-10}	3.0×10^{-9}
Average particle-particle collision energy [J]	9.3×10^{-12}	3.1×10^{-13}

As was seen in Table 4.3 for the L-bend, the number of collisions is higher for Ω -Particles than for Ω -Parcels. The particle-wall collision energy is one magnitude larger and the particle-particle collision energy is one magnitude lower for Ω -Parcels, compared to Ω -Particles. Finally, the results regarding the wall concentration of fine particles are very similar to what was found for the L-bend cases with particles and parcels.

4.1.5 Surface energy

A sensitivity analysis of the surface energy was conducted since the surface energy of the drug formulation used in the experiments was considered to be a factor of uncertainty. Therefore, to broaden the comparison of the results for the base cases and the experiments, a formulation with a higher surface energy was also simulated. All other properties, such as amount of carrier particles and the use of parcels, were the same as for the bases cases, respectively. A higher surface energy leads to fewer fine particles being released upon a collision and increase the possibility of carrier particles agglomerating or adhering to the walls. Since changing the value of the surface energy affects both the fine particles and the carrier particles, results are presented for the fine particles and carrier particles for both sensitivity analysis cases: L-Hakamer and Ω -Hamaker.

L-Hamaker

Figure 4.17 shows the cumulative number of carrier particles emitted from the geometry over the simulated flow time.

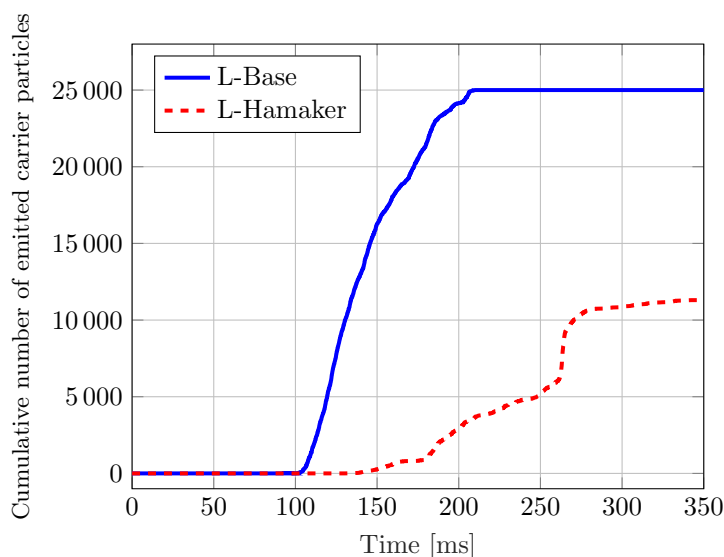


Figure 4.17: Cumulative number of carrier particles emitted from the geometry over time for L-Base and L-Hamaker.

In Figure 4.17 it can be seen that much fewer carrier particles left the geometry for the case L-Hamaker compared to the case L-Base (11 300 carrier particles compared to 25 000). It can also be seen that the carrier particles left the geometry later when the surface energy was increased, and not as continuously as for the base case. The large retention in the case L-Hamaker is shown in Figure 4.18. It can be seen that the parcels with carrier particles are located at the indentation. Further, one parcel have attached to the wall close to the outlet.

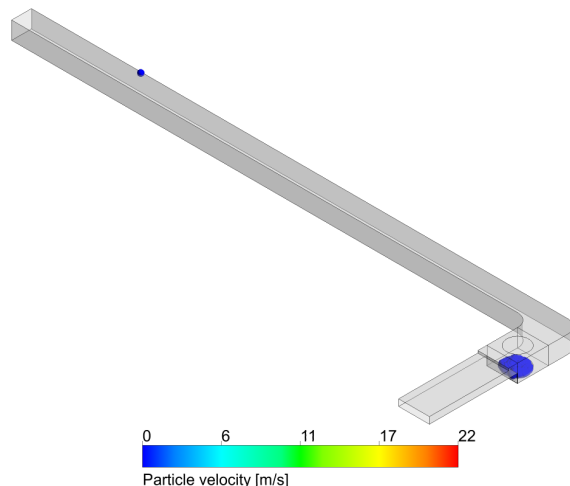


Figure 4.18: Position and velocity of the carrier particles grouped in parcels for the case L-Hamaker at time $t=350$ ms to illustrate the retention of carrier particles.

The large retention of carrier particles also affected the outcome of the fine particles, which are compared for the two cases L-Base and L-Hamaker in Figure 4.19.

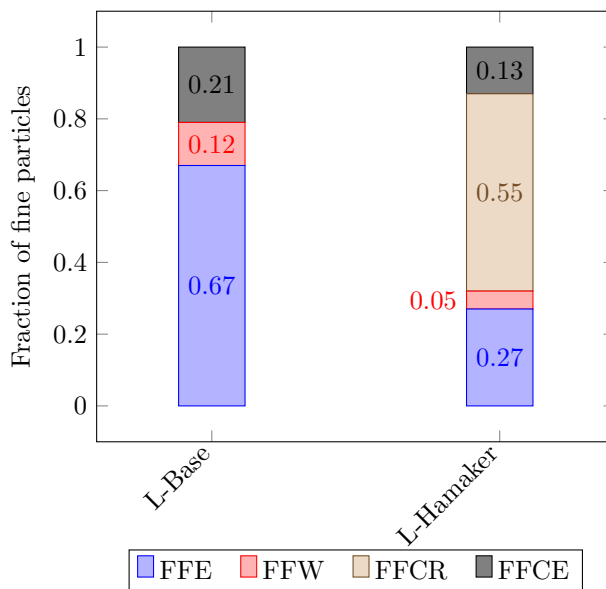


Figure 4.19: The outcome of fine particles for the cases L-Base and L-Hamaker at time $t=350$ ms. FFE is the fraction of emitted fine particles, FFW the fraction of fine particles attached to wall, FFCR and FFCE the fraction of fine particles attached to retained carrier particles and emitted carrier particles, respectively.

In Figure 4.19, it can be seen that the large retention made the fraction of fine particles attached to carrier particles retained in the geometry reach 55 % for L-Hamaker, while it was 0 % for L-Base. This corresponds to a relative decrease of 62 % when the surface energy is taken as five times larger. Further, the fraction of fine particles emitted is much lower for L-Hamaker, see FFE. The fraction of fine particles attached to the walls

and the fraction of fine particles on the carrier particles which exited the geometry are more similar between the two cases, see FFW and FFCE.

For both geometries the most important mechanism for detachment of fine particles is particle-wall collisions. For L-Hamaker, 99.2 % of the fine particles to detach did so due to particle-wall collisions. The remaining 0.8 % detached due to particle-particle collisions.

The results in terms of collisions and collision energy is presented in Table 4.5. It can be seen that the median number of collisions for the carrier particles is much lower for L-Hamaker compared to the corresponding value for L-Base, 24. However, the median number of collisions per emitted carrier particle is higher than of the total carrier particles, and therefore more similar to the base case. The total number of collisions are significantly higher for L-Base than for L-Hamaker, for both type of collisions: the number of particle-particle collisions are almost five times larger and the number of particle-wall collisions almost four times larger for L-Base than for L-Hamaker. However, the average collision energy is higher for both type of collisions when the surface energy is increased: for particle-particle collisions it increase with a factor six and for particle-wall collisions with a factor of almost five.

Table 4.5: Summary of results in terms of collisions and collision energy for L-Hamaker.

	L-Hamaker
Median number of collisions per carrier particle	4
Median number of collisions per emitted carrier particle	13
Number of particle-wall collisions	62 340
Number of particle-particle collisions	114 140
Average particle-wall collision energy [J]	2.7×10^{-9}
Average particle-particle collision energy [J]	9.7×10^{-13}

Figure 4.20 shows the concentration of fine particles attached to the walls for L-Hamaker. The highest concentration is located at the bend, see Figure 4.20b. Compared to the base case, see Figure 4.8, it can be seen that the concentration is lower and spread out over fewer cells for L-Hamaker. This is due to the lower number of particle-wall collisions for L-Hamaker compared to L-Base. Also, in Figure 4.20b it can be seen that there is no zone of high concentration of fine particles at the wall and bottom of the indentation, as can be seen for L-Base, see Figure 4.8b.

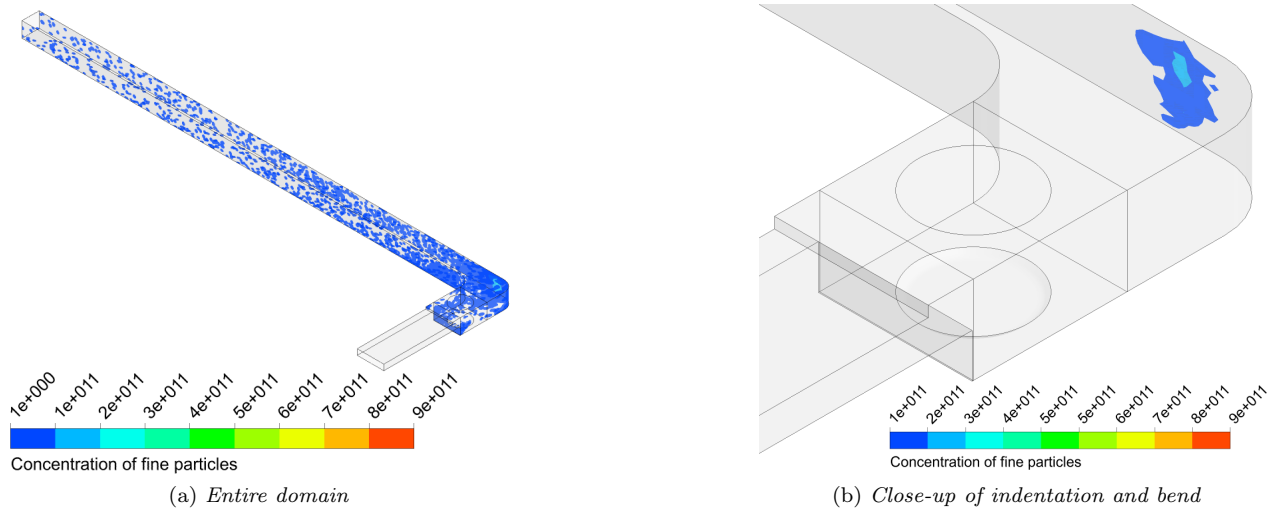


Figure 4.20: Concentration of fine particles attached to the walls for $t=350$ ms for the case L-Hamaker. The concentration is defined as number of fine particles per unit area.

Summarizing, it can be concluded that increasing the value of the surface energy has a large impact on the results for the L-bend geometry. The retention of carrier particles become much higher, which also affects

the results for the fine particles: the fraction of emitted fine particles significantly decreases when the surface energy is increased.

Ω -Hamaker

The cumulative number of carrier particles leaving the geometry over time is shown in Figure 4.21 for Ω -Base and Ω -Hamaker. It can be seen that there is a significant difference between the two cases: the retention of carrier particles was much higher for Ω -Hamaker, only 710 carrier particles left the geometry compared to 22 220 for Ω -Base. Also, it can be seen that the carrier particles which left the geometry, did so approximately 50 ms later than when the last carrier particles left the geometry in Ω -Base.

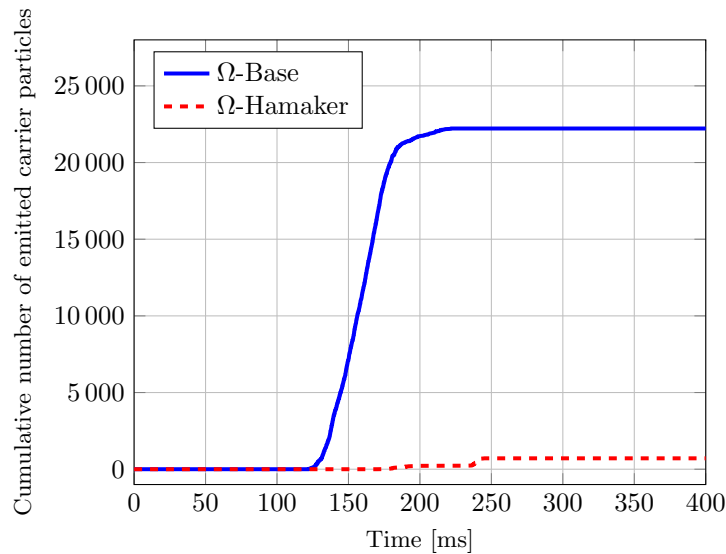


Figure 4.21: *Cumulative number of carrier particles emitted from the geometry over time for Ω -Base and Ω -Hamaker.*

The retention of carrier particles for Ω -Hamaker can be seen in Figure 4.22. The parcels with carrier particles are located at the indentation, except for two parcels which have attached to the walls before the first bend and the outlet, respectively. A difference in the location of the retention can be seen compared to the base case, see Figure 4.9d, where the parcels are positioned more towards the step.

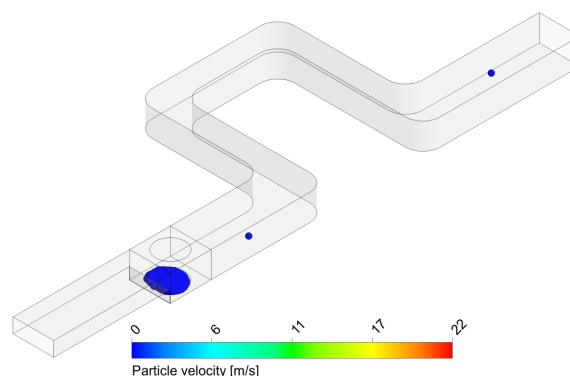


Figure 4.22: *Position and velocity of the carrier particles grouped in parcels for the case Ω -Hamaker at time $t=400$ ms to illustrate the retention of carrier particles.*

The large retention of carrier particles also affected the outcome of fine particles for Ω -Hamaker, which can be seen in Figure 4.23. The number of fine particles attached to carrier particles retained in the geometry

was 98 % of the total number of fine particles, compared to 11 % for Ω -Base. This corresponds to a relative decrease of 97 % when the surface energy was taken as five times larger. Since such a large fraction of the fine particles was attached to the carrier particles still retained in the geometry, only a minor part of the fine particles were emitted and none were attached to the walls. This shows a large difference compared to Ω -Base, where a majority of the fine particles were emitted and a small part was attached to the walls. Similarly to the Ω -Base case, there was no fraction of fine particles attached to the carrier particles emitted from the geometry for Ω -Hamaker.

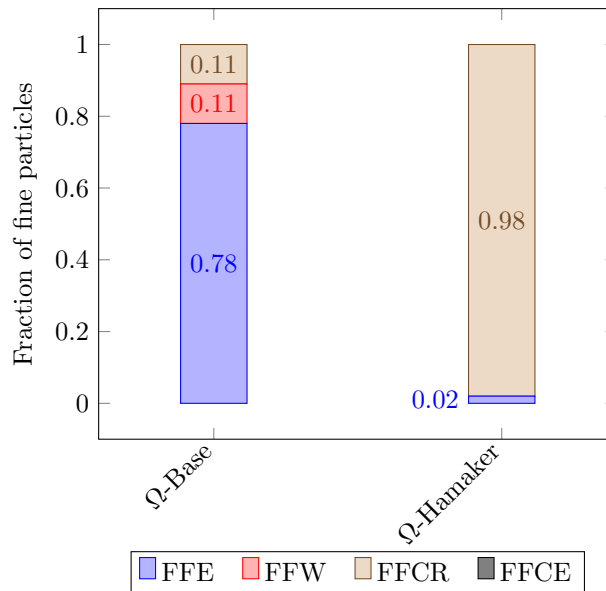


Figure 4.23: *The outcome of fine particles for the cases Ω -Base and Ω -Hamaker at time $t=400$ ms. FFE is the fraction of emitted fine particles, FFW the fraction of fine particles attached to wall, FFCR and FFCE the fraction of fine particles attached to retained carrier particles and emitted carrier particles, respectively.*

As for the base case, particle-wall collisions caused the majority, 99.4 %, of the emitted fine particles to be detached. The remaining 0.6 % were detached due to particle-particle collisions. The number of collisions and the average collision energy is presented in Table 4.6. A large difference for the median number of collisions is found between the cases Ω -Base and Ω -Hamaker, 1 compared to 46. However, the median number of collisions per emitted carrier particle is larger than if all carrier particles is included, around half of that for the base case. Also the total number of collisions are lower for Ω -Hamaker: the number of particle-particle collisions is thirty times larger and the number of particle-wall was forty for Ω -Base, respectively. However, the average collision energy is similar for the two cases.

Table 4.6: Summary of results in terms of collisions and collision energy for Ω -Hamaker.

	Ω -Hamaker
Median number of collisions per carrier particle	1
Median number of collisions per emitted carrier particle	22
Number of particle-wall collisions	11 120
Number of particle-particle collisions	27 990
Average particle-wall collision energy [J]	4.9×10^{-9}
Average particle-particle collision energy [J]	4.3×10^{-13}

The concentration of fine particles attached to the walls of the geometry can be seen in Figure 4.24. As an effect of the large retention of carrier particles and fewer collisions, the number of fine particles attached to the walls is much lower for Ω -Hamaker than for Ω -Base. Further, no zone with a relatively high concentration can be seen at the indentation. Instead, the highest concentration is found at the wall of the first bend.

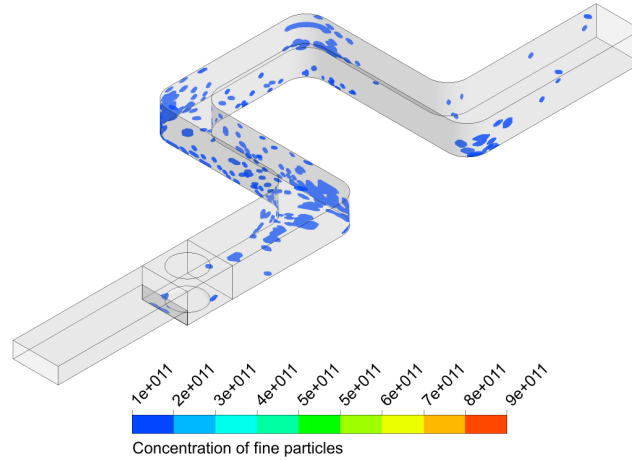


Figure 4.24: Concentration of fine particles attached to the walls for $t=400$ ms for the case Ω -Hamaker. The concentration is defined as number of fine particles per unit area.

Summarizing, changing the value of the surface energy has an even larger impact on the results for the Ω -bend geometry than it does for the L-bend geometry: the retention is very large, 97 % of the carrier particles did not leave the geometry, and the fraction of fine particles emitted was only 2 %.

4.1.6 Diffusion

In this section, the results for the sensitivity analysis of the diffusion coefficients in the scalar transport equations are presented for the L-bend and the Ω -bend. Changing the diffusion coefficients only affects the transportation of fine particles and not the DEM-solution for the carrier particles. Hence, no results are presented for the carrier particles, since these are the same as for the base cases presented in section 4.1.3.

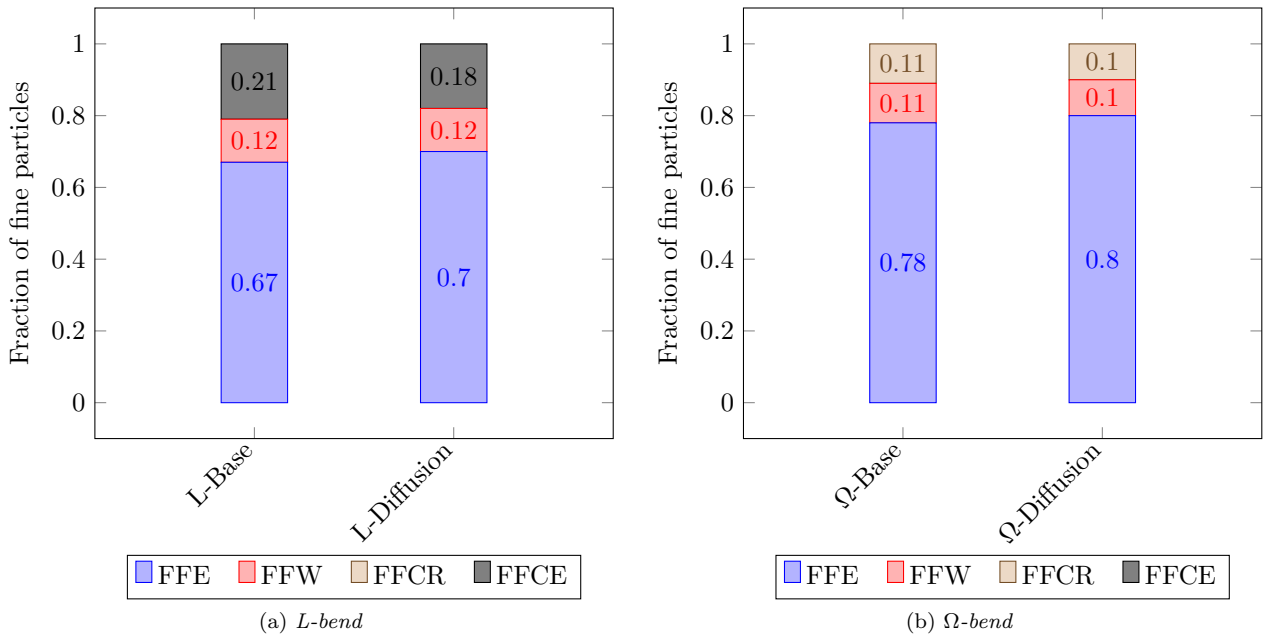


Figure 4.25: The outcome of fine particles for the cases a) L-Base and L-Diffusion at time $t=350$ ms and b) Ω -Base and Ω -Diffusion at time $t=400$ ms. FFE is the fraction of emitted fine particles, FFW the fraction of fine particles attached to wall, FFCR and FFCE the fraction of fine particles attached to retained carrier particles and emitted carrier particles, respectively.

The outcome of fine particles for L-Diffusion compared to L-Base can be seen in Figure 4.25a and Ω -Diffusion compared to Ω -Base in Figure 4.25b. As can be seen, there is a negligible difference for the outcome of fine particles between the two cases for the L-bend and the two cases for the Ω -bend. The results indicate that increasing the diffusion coefficients in the scalar transport equations with an order of three magnitudes, does not affect the results for either geometry.

4.2 Experimental results

As mentioned in section 3.3.2, the properties measured in the experiments were the mass of the loaded dose, the mass of emitted fine particles, the mass median aerodynamic diameter (MMAD) of emitted fine particles, the pressure drop and the mass of powder retained in the geometry. In the experiments, loading a dose that was similar in terms of mass for all test was difficult, and the values range from 4.6 mg to 13.1 mg. The averaged mass of the initial dose over all tests is 8.9 mg. To ease the comparison of different tests, because of the variability in loaded mass, the mass of emitted fine particles is presented as fraction of the initial dose of fine particles (FFE) and the mass of Retained Dose as Fraction of the initial dose (RDF). The results presented in this section are averaged for each copy over the tests performed on it. For some important results also the Relative Standard Deviation (RSD) is presented. The complete results for each test can be found in Appendix B. The averaged results for the L-bend copies are presented in Table 4.7.

Table 4.7: Summary of averaged results for the tests on the L-bend device copies including the relative standard deviation (RSD). FFE is the fraction of emitted fine particles, RDF is the retained dose fraction and MMAD is the mass median aerodynamic diameter of emitted fine particles.

	L1	L2	L3
Loaded drug dose [mg]	8.1	7.7	9.3
RSD of loaded drug dose	0.39	0.31	0.1
FFE	0.34	0.43	0.45
RSD of FFE	0.39	0.48	0.4
RDF	0.14	0.12	0.21
RSD of RDF	0.60	0.94	0.27
MMAD [μm]	1.92	1.85	1.83
RSD of MMAD	0.06	0.03	0.01

For the L-bend copies, the MMAD is relatively constant between the tests and only has a RSD of maximum 0.06. The averaged pressure drop of the copies of the L-bend device is also relatively constant and range between 3.3 kPa and 3.9 kPa. The first test on L2, the second copy of the L-bend, is the test that has the largest variation among all test on the L-bend copies. Overall, the L-bend copies have high RDS for the results of FFE and RDF. Visually, it could be noticed in several test that some powder was retained at the bottom, close to the corners of the backwards facing step.

The averaged results for the Ω -bend can be seen in Table 4.8. It can be see that the results for the second copy has lower fraction of emitted fine particles FFE and higher retained dose fraction RDF compared to the other copies of the Ω -bend.

Table 4.8: Summary of averaged results for the tests on the Ω -bend device copies including the relative standard deviation (RSD). FFE is the fraction of emitted fine particles, RDF is the retained dose fraction and MMAD is the mass median aerodynamic diameter of emitted fine particles.

	$\Omega 1$	$\Omega 2$	$\Omega 3$
Loaded drug dose [mg]	8.7	9.5	10.3
RSD of loaded drug dose	0.24	0.37	0.29
FFE	0.41	0.33	0.39
RSD of FFE	0.20	0.37	0.11
RDF	0.12	0.19	0.10
RSD of RDF	0.64	0.70	0.60
MMAD [μm]	1.80	1.83	1.81
RSD of MMAD	0.06	0.04	0.06

Similarly to the results for the L-bend device, the MMAD is consistent between the tests and only has a maximum RSD of 0.06. The averaged pressure drop of the copies of the Ω -bend device is also relatively constant and ranges between 2.2 kPa and 2.3 kPa. As for the L-bend device, in several tests some powder seemed to be retained at the bottom close to the corners of the backwards facing step. Looking at the second copy of the Ω -bend device after the first testing, it could be seen that a trace of powder was left on the bottom of the device, possibly due to wax residues. This result is an outlier compared to the other results for the Ω -bend copies as it has much higher retention and fewer emitted fine particles.

Finally, the averaged results of the L-bend and Ω -bend devices are compared in Table 4.9. It can be seen that FFE is slightly larger for the L-bend but also shows more variability. The retained dose fraction is similar for the L-bend and the Ω -bend.

Table 4.9: Summary of the averaged results for the tests on the L-bend and Ω -bend devices, including the relative standard deviation (RSD). FFE is the fraction of emitted fine particles, RDF is the retained dose fraction and MMAD is the mass median aerodynamic diameter of emitted fine particles.

	L-bend	Ω -bend
Loaded drug dose [mg]	8.4	9.5
RSD of loaded drug dose	0.26	0.27
FFE	0.41	0.38
RSD of FFE	0.32	0.22
RDF	0.16	0.14
RSD of RDF	0.55	0.67
MMAD [μm]	1.87	1.81
RSD of MMAD	0.04	0.05

As previously mentioned, the second copy of the L-bend, L2, has a large variability in results compared to the other L-bend copies and the second copy of the Ω -bend, $\Omega 2$, with the trace of wax at the bottom, retained more powder than the other Ω -bend copies. If the outlying test for these two copies are omitted from the results in Table 4.9, the results in terms of FFE and RDF become: 0.37 and 0.18 for the L-bend, and 0.40 and 0.11 for the Ω -bend.

As mentioned in section 3.3.2, one copy of the L-bend and one copy of the Ω -bend were used to visualize the flow of the powder in the experiments. The camera used only had a capability of 20 frames per second, which, together with the fact that the roofs of the devices were not completely transparent, yielded unclear results.

4.3 Comparison of numerical and experimental results

Part of the scope of this master's thesis is to compare the results for the numerical simulations and for the experiments. Therefore, in this section some important results from section 4.1 and section 4.2 are highlighted and compared. The results from the experiments are comparable with the base case simulations and the

sensitivity analyses of the surface energy and diffusion coefficients in the scalar transport equations, (see sections 4.1.3, 4.1.5 and 4.1.6). This is because the size of the drug dose in these cases is similar. The doses are 7.1 mg in the numerical simulations mentioned above and 8.9 mg averaged in the experiments. Since the results for the base cases and the sensitivity analysis of the diffusion coefficients are very similar, the latter are not presented in this section.

The pressure drop in the simulations is 2.0 kPa for the Ω -bend and 3.0 kPa for the L-bend. The pressure drop in the experiments is slightly higher for the Ω -bend, around 2.2 kPa, and higher for the L-bend, averaged to 3.6 kPa for all copies. That is, in terms of relative pressure drop, the numerical simulations yield 17 % and 9 % lower pressure drop for the L-bend and Ω -bend compared to the experiments. In order to be able to compare the retention of powder, the results of the simulations need to be translated in terms of retained dose fraction. The retained dose in the simulations consists of carrier particles retained, fine particles attached to walls and fine particles attached to carrier particles retained.

A comparison of the results for the fraction of fine particles emitted FFE and the retained dose fraction RDF can be seen in Table 4.10. FFE is highest for the base case simulations, and lowest for the sensitivity analyses of the surface energy. The experimental results lie in between. Regarding the RDF, most retention can be seen in L-Hamaker and Ω -Hamaker, while the base case simulations have the least retention. Again the experimental results lie in between. The retention of the drug dose for the Ω -bend is very similar in the experiments and in the Ω -Base simulation.

Table 4.10: Summary of the results of the numerical simulations and of the averaged results of the experiments, for both the L-bend and the Ω -bend. FFE is the fraction of emitted fine particles and RDF is the retained dose fraction.

	L-bend			Ω-bend		
	L-Experiment	L-Base	L-Hamaker	Ω-Experiment	Ω-Base	Ω-Hamaker
FFE	0.41	0.67	0.27	0.38	0.78	0.02
RDF	0.16	0.0	0.55	0.14	0.12	0.97

In the experiments, it could visually be seen that for some tests a bit of white powder was retained at the backwards facing step towards the inlet. This is also the case for the Ω -Base simulation. In L-Base no powder was retained and in L-Hamaker and Ω -Hamaker the carrier particles mostly attached to the indentation as could be seen in Figure 4.18 and 4.22.

5 Discussion

The aim of this master's thesis was to investigate a computationally affordable modeling approach of carrier-based drug formulations in DPIs. The fluid phase and carrier particles were modeled with CFD-DEM in the commercial software Fluent. This was thereafter coupled with micro-models for the fine particles. Further, the numerical simulations were also compared with results of experimental testing. The micro-models are believed to have been adequately implemented and coupled to the CFD-DEM solver since the fine particles behaved in accordance with the observed dynamics of the carrier particles. In this chapter, the results presented in chapter 4 are discussed and analyzed. First, this is done for the results of the numerical simulations and second for the experimental results. Thereafter, the two sets of results are evaluated and analyzed.

5.1 Simulations

In this section, first the results of the two base cases are compared and analyzed. Then, the results of the sensitivity analyses are evaluated to broaden the conclusions of the numerical simulations. Finally, error sources for the numerical simulations are presented.

5.1.1 Base case simulations

Two geometries were designed to yield different results in terms of fraction of emitted fine particles to evaluate the implementation of the micro-models and compare the results of the simulations with the experimental testing. To obtain the desired difference, four bends were included for the Ω -bend geometry. This was thought to increase the number of collisions for the carrier particles, compared to the L-bend geometry which have one bend. A higher number of collisions should implicate a larger fraction of emitted fine particles. A difference in terms of number of collisions between the two geometries was accomplished: the median number of collisions is around twice as large for the Ω -bend. Further, the average collision energy for both particle-particle and particle-wall collisions is higher for the Ω -bend. It is believed that the higher particle-wall collision energy for the geometry Ω -bend is due to the longer distance to the first bend. This gives the carrier particles a longer time to accelerate with the flow and therefore they collide with a larger velocity.

It was also the average particle-wall collision energy which was found to be the largest for both geometries. This indicates that in average, the impact velocity upon wall collisions is higher than the impact velocity when the carrier particles collide with other particles.

As desired, a difference was achieved for the fraction of fine particles emitted, of 11 percentage points, for the two geometries in the numerical simulations. However, the difference was not large enough to give conclusive results for the experimental testing. Therefore, a larger difference between the result for the two geometries is desired. A larger difference could be generated by decreasing the fraction of emitted fine particles in the L-bend. This could be done by increasing the inlet area. An increased area of the inlet would have given a lower inlet flow velocity for a given flow rate. Therefore, the carrier particles would also have had a lower velocity. With a lower velocity of the carrier particles, less fine particles would have been detached upon collisions and the fraction of emitted fine particles would have decrease. The impact velocity of wall collisions at the bend, which are believed to be the largest source of detachment of fine particles in the L-bend, could possibly had been decreased further if a 90° bend was not used, since that would have decreased the wall normal velocity. In addition, decreasing the height of the backward facing step should have eased the release of carrier particles from the indentation. This would further have decreased the impact velocity of the parcels with the walls, since they would have been released at an earlier stage when the flow velocity is lower.

Of the three detachment mechanisms, particle-wall collisions showed to be the most important for detachment of fine particles in both geometries. Of the detached fine particles, more than 98 % were caused by impacts with the walls of the geometry. The remaining part was detached upon particle-particle collisions, but this can be neglected in comparison with particle-wall collisions. The dispersion of fine particles due to drag force acting on the carrier particles was found to not contribute at all to the detachment of fine particles, at the simulated surface energy. Which detachment mechanism that is the most important seems to be dependent on

the geometry. In the previous study by Tong et al. [2], the particle-wall collisions was also found to be the most important detachment mechanism. The geometry used there is more complex than the two geometries used in this study, but it showed the same results. However, a study by Wachem et al. [1] states that the particle-particle collisions is the most important detachment mechanism. The geometry used in that study is more comparable with the geometry used in this work, especially the L-bend, but the drug dose was placed differently: it was placed after the bend. This implies that the impact velocity for particle-wall collisions would be low, since the impact velocity is taken as the wall normal velocity. Further, it is believed that the number of particle-wall collisions was much lower in the work by Wachem et al. than in this study, and consequently the particle-wall collisions became a much less important detachment mechanism.

5.1.2 Sensitivity analyses

As previously stated, three parameters were investigated in the sensitivity analyses: the use of parcels, the value of the surface energy and the value of the diffusion coefficients in the scalar transport equations. The results of the sensitivity analyses are discussed below.

Comparison of particles and parcels

To save computational power, the carrier particles were grouped into parcels. However, to ensure that the results are accurate, the use of parcels must be evaluated. Comparing the cases with particles and the cases with parcels, the behaviour of the carrier particles seems to be correctly captured when parcels are used and the accuracy appears to increase with increased number of carrier particles simulated. For the cases with 1000 carrier particles and 100 parcels, a different trend than for the base cases can be seen regarding the total number of collisions: when only 1000 carrier particles are simulated, the number of particle-wall collisions is higher than the number of particle-particle collisions. This appears to be reasonable since the possibility of particle-particle collisions decrease with decreasing number of particles. Further, the median number of collisions decrease when parcels are used.

Regarding the outcome of fine particles, the fraction of fine particles emitted is higher for the cases with parcels. Since the median number of collisions for the carrier particles is lower when parcels are used, it indicates that more fine particles are emitted with fewer collisions. This corresponds to that the parcels with carrier particles must collide with a larger impact velocity than the carrier particles. This is also confirmed by the higher average particle-wall collision energy for the cases where parcels are used to model the carrier particles. An explanation for the higher impact velocity at wall collisions could be that the parcels are less disturbed by particle-particle collisions. Hence, they can be accelerated by the flow to a higher velocity, which would increase the impact velocity.

For all cases in this sensitivity analysis particle-wall collisions were found to be the most important detachment mechanism, equal to what was found for the base cases. However, it was found to be more important in the cases where parcels with carrier particles were used than in the case with individual particles. The difference was the largest for the cases with 10 000 particles. This indicates that the use of parcels slightly underestimates the importance of particle-particle collisions. Therefore, the particle-particle collisions could be more important than what was reported for the base case simulations. However, particle-wall collisions are still believed to be the most important mechanism.

The wall concentration was found to be lower for the cases where parcels with carrier particles were used. Also the fraction of fine particles attached to the walls is lower for the cases with parcels. This seems reasonable since also the number of particle-wall collisions is lower.

In summary, the use of parcels to model the carrier particles show some difference in results, compared to when the carrier particles are modeled individually. However, these differences appear to be small enough to conclude that the behaviour of the carrier particles is captured with the use of parcels.

Surface energy

An analysis of the sensitivity to the value of the surface energy was conducted since the surface energy of the drug formulation used in the experiments was thought to be a factor of uncertainty. For the cases where the surface energy was increased by a factor of 5, a large difference compared to the base cases was found with regards to retention of carrier particles, especially for the Ω -bend. The larger difference for the Ω -bend is believed to be caused by the lower maximum inlet velocity (the inlet velocities over time for the two geometries is presented in Figure 3.7). The large retention highly affects the median number of collisions. However, the median number of collisions for the emitted carrier particles was found to be much more similar to the values obtained for the base cases. The difference is believed to be due to fewer particle-particle collisions, due to fewer carrier particles being released from the indentation. The more similar results in number of collisions for the emitted carrier particles indicates that they collide in a similar way to what was seen for the base cases. On the other hand, the average collision energy was found to be higher for both particle-particle and particle-wall collisions when the surface energy is increased. This means that in average, the parcels with carrier particles collide with the walls and with other parcels with a higher velocity compared to the base cases. This is believed to be caused by the fact that the parcels left the indentation later when the surface energy is increased. At a later time, the fluid flow has reached a higher velocity which would also increase the velocity of the carrier particles. This could also explain the lower median number of collisions for the carrier particles if the parcels follow the flow to a greater extent.

The concentration of fine particles attached to the walls differed between the base cases and the cases with the higher surface energy: the number of fine particles attached to the walls was less when the surface energy was increased, due to the large retention of carrier particles.

The relative decrease of the fraction of fine particles emitted was found to be large, especially for the Ω -bend, when the surface energy was increased by a factor of 5. This has previously been investigated in the study by Wachem et al. [1] where it was found that the relative decrease was 25 % and hence much smaller than in this work. The difference in results between this work and the previous study is believed to be induced by the indentation used in this study. The indentation seems to be a large obstacle for the release of carrier particles from injection position when the surface energy is increased. As a consequence, the number of collisions for the carrier particles are significantly decreased, which in turn decreases the fraction of fine particles emitted substantially.

In summary, some large differences were found between the base case simulations and the simulations with increased surface energy. This indicates that the results of this sensitivity analysis should be used to broaden the comparison of the results from the simulations and the experiments.

Diffusion coefficients

The sensitivity to the value of the diffusion coefficients in the scalar transport equations was investigated. An increase by three orders of magnitude did not show any difference for the results. Hence, the assumption that diffusion is a negligible transport mechanism compared to convection is believed to be reasonable. This indicates that with regards to the diffusion coefficients, the results of the base case simulations should be comparable with the results of the experimental testing.

5.1.3 Error sources

A computational mesh independence study was conducted in order to ensure that a proper mesh was used in the simulations. However, the study was performed for a single phase flow: only the fluid phase was included. Therefore how the carrier particles affect the flow was not taken into account. It could be expected that the larger the number of carrier particles, the more they should affect the flow. Consequently, if this would cause some errors in the simulations, they are expected to be largest for the cases with 25 000 carrier particles. However, this error is believed to be small since the same pressure drop was obtained in the base cases and the cases without particles.

Further, with the limited time frame of this work, sensitivity analyses were only conducted on some parameters believed to have the largest effect on the results. No solver settings were investigated. An analysis of the

solver settings could include investigating the choice of model for the contact forces in the DEM-solver, turbulence model, discretization schemes, under-relaxation factors and wall roughness. In the simulations, the wall roughness was modeled with a default constant value. Therefore, it is not known if the value used is representative of the wall roughness in the experiments.

Another possible error source could be the initialization of the fluid flow. Since the time frame for the simulations are so small, 350 and 400 ms, respectively, and the velocity increases over time it is probable that the initialization of the fluid flow could have a large impact on the results. In addition, it was not investigated how the initialization of the injection of carrier particles affects the results. It could be interesting to determine how the drug dose should be injected in the simulations to best mimic the experiments in terms of shape of the injection (in this work a cylindrical form was used) and the bulk density. The distance between the parcels is especially believed to affect the agglomeration, since the adhesive force is a function of it.

5.2 Experiments

In this section the experimental results presented in section 4.2 are discussed and evaluated. As could be seen from the relative standard deviation in Table 4.7 and Table 4.8, the results varied considerably over the three testings performed on each of copy. The L-bend had the largest variance in the results for the fraction of emitted fine particles. The Ω -bend had less variation when looking at the fraction of fine particles emitted. When looking at the retained dose fraction, both the L-bend and the Ω -bend showed large variations, but had a similar averaged retained dose fraction. The L-bend and the Ω -bend also presented very similar averaged values of fraction of fine particles emitted. This is unwanted since the devices have been designed with the intention of yielding sufficiently different performances in terms of emitted fine particles to be captured qualitatively in the experimental testings. If the outlying results for the second copies of the L-bend and the Ω -bend are discarded, the Ω -bend yields 3 percentage points higher fraction of fine particles emitted as mentioned in section 4.2. Suggestions on how the design of the geometries can be modified to yield a larger difference in results are mentioned in section 5.1.1 above.

As a final remark before looking at the error source arising from the experimental testing, it should be considered that the experimental devices were only designed to be representative of real inhalers in terms of pressure drop. The properties of the material and the distinct patterning related to the 3D-printing process are probably not descriptive of material properties and wall roughness for real inhalers.

5.2.1 Experimental error sources

The reasons behind the large variability in the results are an issue that is not fully understood and probably depends on the interaction of various aspects. Some causes may be related to the 3D-printing process: the surfaces of the devices presented patterning derived from the 3D-printing process. Since the patterning was quite deep and ridged, it can affect the results in terms of wall surface roughness. A more smooth surface could be obtained by grinding the inner surfaces of the devices or by using a 3D-printer with a higher precision to print out the devices. Further, as was explained in Table 3.4, the bottom of the devices presented different directions of patterning depending on how they were oriented in the 3D-printer. L3, the third copy of the L-bend had a different patterning compared to the other L-bend copies. It was directed orthogonal to the flow direction over most of the device (V-pattern). The L3 copy did in fact retain in average twice as much powder compared to the other L-bend copies, which could be caused by the patterning. Also Ω 2, the second copy of the Ω -bend, had a different patterning compared to the other copies. This patterning was directed parallel to the flow field in most of the device (H-pattern). Based on how the V-pattern affected the results of the L-bends, the H-pattern in the Ω -bend device could be expected to generate less retention. However, during the experiments, a trace of powder was found at the bottom of this copy, indicating that some wax from the 3D-printing process still was present. This can explain the higher retention of powder seen for this copy compared to the other Ω -bend copies which were V-patterned.

The devices were designed so that the different components adhered tight to each other to avoid leakage. However, some variability was seen in the results for the different copies, among others for the pressure drop of the L-bend copies. Leakage, and different amounts of leakage between different copies, could be one of the

explanations for the variability in the results. Further, as the devices created only were desired to have an appropriate pressure drop and similar performance in terms of released fines, the pressure drop over the L-bend and the Ω -bend could have been made more similar, in order to reduce the amount of uncertain factors that affect the results. Possible error sources also arise from the experimental testing procedure. Placing the dose correctly in the indentation was challenging and yielded different outcomes both in terms of location and mass of the drug dose for all the tests. Further, handling the devices during testing without dislocating the drug dose from the indentation was also difficult, since the indentation was too shallow to fully prevent the drug dose from moving around. The instrumentation could also affect the accuracy of the experimental results. The values measured by the scale used to weight the devices before and after testing did sometimes oscillate, which raises questions concerning the accuracy of the weighting. This would affect both the results in terms of FFE and RDF.

5.3 Comparison of simulations and experiments

As emphasized again in the beginning of this chapter, the aim of this master's thesis was to implement the micro-models in commercial software and evaluate the work by comparing simulations and experiments. Therefore the results of the numerical simulations and the experiments, summarized in section 4.3, are discussed in this section. To begin with, the pressure drops over the devices measured in the experiments were very similar to those obtained in the simulations. This indicates that the flow field was well resolved in the simulations.

Further, it was seen in Table 4.10, that the retention of drug powder in the devices was very similar between the experiments and the base case for Ω -bend. The L-Base simulation had no retention. The reasons behind these differences for the numerical and experimental results for the L-bend are not clear. The patterning on the bottom surface gave high retention for the third copy of the L-bend, L3. The other two copies had less retention, but high variability in the results, with RDF ranging from 0.0 to 0.27. This indicates that more experimental testing is needed to get coherent results after determining how differences in patterning, wall roughness, wax residues and leakage between the copies may affect the outcome.

In Table 4.10, it was seen that the base case simulations yielded a much higher fraction of fine particles emitted (FFE) compared to the experiments. That the numerical and experimental results for FFE would yield different results was not surprising considering the experimental uncertainties mentioned in section 5.2. In fact, one of the objectives was to design the geometries so that they would yield sufficiently different results in terms of FFE to be qualitatively captured in the experiments. The difference between the L-bend and the Ω -bend in the base case simulations was only 11 percentage points and in the experiments, after removing the outlying tests as mentioned in section 4.2, only 3 percentage points. This indicates that the desired qualitative difference was not reached. Designing the geometries so to yield more difference in terms of FFE would have given more conclusive results in the experimental testing.

Since the visualization of the powder emitting from the device gave poor results in the experimental testing, the height of the backward facing step could be decreased. As implied in section 5.1.1, this could increase the difference in amount of fine particles emitted between the two geometries.

Finally, for both geometries, the results of the experiments lie between the simulations of the base cases and of the sensitivity analysis of the surface energy. As increasing the surface energy five times affected the results of the simulations considerably, we believe that even small variations in the material properties of the drug formulation and of the walls could affect the experimental results. This indicates that careful assessment of the material properties, both for the walls of the studied device and for the tested drug formulation, is needed to obtain adequate results from the numerical simulations, .

5.3.1 Limitations of the micro-models

The given micro-model may not describe all relevant processes involving the fine particles in the experimental testing, since they only describe the attachment of fine particles to walls as a carrier particle impacts upon a wall and the detachment of fine particles due to collisions and drag dispersion.

To start with, the fine particles dispersed in the air flow can agglomerate due to strong adhesive forces. If agglomeration was present to a large extent in the experiments, the fine particles may have combined into large agglomerates that the APS would not have measured as FFE. This would underestimate the number of fine particles emitted. Further, the fine particles in the air flow may have attached to walls, or re-attached to other carrier particles. Another possible mechanism, that could have caused the re-attachment of fine particles to a carrier particle, is the impact of a carrier particle against a wall covered with fine particles due to prior collisions. None of these processes is described by the micro-models implemented in this master's thesis. We believe that fine particles in air attaching to the walls may be a relevant process to include in the modeling approaches for fine particles in the studied case.

5.4 Future work

From the findings in this master's thesis, some future research areas can be suggested. To improve the possibilities for validating the simulations with experimental testing, some modifications to the experimental testing devices can be applied by decreasing the surface roughness, the patterning and the possible leakage. The design of the devices can also be modified so to increase the difference in amount of fine particles emitted for the two geometries tested. It would also be interesting to perform experiments on a drug formulation with a higher surface energy and see if it would affect the results in a way similar to what was seen in the numerical sensitivity analysis.

In order to evaluate the accuracy of the numerical simulations, a thorough analysis of the solver settings for the CFD-DEM solver could be performed. Some of the models and settings in the simulations that could be interesting to investigate are the turbulence model, wall roughness and DEM collision model. Further, changing how the carrier particles are initialized in the geometry could possibly better mimic the experiments.

Future development can also be driven in terms of modeling of fine particles, depending on which mechanisms are believed to be important for predicting the performance of DPIs. Because of the surface roughness and patterning of the 3D-printing devices used in the experimental testing, the formulation and implementation of a micro-model for the adhesion of fine particles in air to walls could be important for the performance prediction. As mentioned in section 5.2, however the 3D-printed devices used in this project are not necessary representative of the wall characteristics of a real inhaler device, meaning that implementing an additional micro-model as the one described above may not be necessary.

Other micro-models that could be interesting to implement could describe the agglomeration of fine particles or, as proposed by Wachem et al. [1], the re-attachment of fine particles to carrier particles moving through air or colliding against a wall covered with fine particles.

6 Conclusions

This project was undertaken to investigate an alternative approach for modeling fine particles in carrier-based DPIs. The approach consists of implementing given micro-models that describe the detachment of fine particles from carrier particles due to three different mechanisms: collisions of carrier particles against walls or other particles and interaction with the fluid phase. Further, the micro-models also include the attachment of fine particles on walls upon particle-wall collisions. The fluid phase and the carrier particles are modelled with CFD-DEM in the commercial software ANSYS Fluent. The modeling approaches used are evaluated by performing numerical simulations on two generic geometries with pressure drops and flow curves relevant for real DPIs. The two geometries were designed to yield a qualitative difference in terms of emitted fine particles. To broaden the numerical study, three sensitivity analyses were conducted. These included investigating the effects of using parcels for modeling the carrier particles, increasing the surface energy and increasing the diffusion coefficients in the scalar transport equations for the fine particles dispersed in the air. Finally, experimental testing on 3D-printed copies of the geometries used in the numerical study was conducted to compare the results with the simulations.

In this master's thesis, the given micro-models for describing the behaviour of fine particles have successfully been implemented and coupled to commercial CFD-DEM software. The numerical results show that increasing the surface energy five times had a large impact on the results. On the contrary, increasing the diffusion coefficients for the transport equation of fine particles with three magnitudes did not affect the results.

The numerical simulations also showed that the two generic devices had different performance in terms of number of fine particles emitted but the difference was too small to be captured in the experimental testing. However, the experimental results showed high variability. Uncertainties in the experimental testing indicate that more effort should be directed to increase the accuracy in measurements and the quality of the 3D-printed devices with respect to wall roughness and leakage. If wall roughness is suspected to be an important factor in the performance of the studied inhaler device, further development of the micro-models could include modeling the adhesion to walls for fine particles dispersed in air. In addition, a larger difference in terms of emitted fine particles could be achieved for the two geometries by modifying the design of the geometry L-bend. For example, the inlet area could be increased to decrease the flow velocity.

In conclusion, the modeling of fine particles with micro-models, and of fluid flow and carrier particles with CFD-DEM, is found to be an affordable alternative to DEM modeling of the complete drug formulation. Depending on the features of the studied device, with some development regarding the mechanisms included in the micro-models, this approach could be introduced in the early stages of product development of DPIs.

References

- [1] B. von Wachem et al. Simulation of Dry Powder Inhalers: Combining Micro-scale, Meso-scale and Macro-Scale Modeling. *AIChE Journal* **63.2** (2017), 501–516.
- [2] Z. Tong et al. Multi-scale Modelling of Powder Dispersion in a Carrier-Based Inhalation System. *Pharmaceutical Research* **32.6** (2014).
- [3] M. R. Tamadondar et al. Numerical Modeling of Adhesive Particle Mixing. *American Institute of Chemical Engineers AIChEJ* **63** (2017), 2599–2609.
- [4] H.P.Zhu et al. Discrete particle simulation of particulate systems: Theoretical developments. *Chemical Engineering Science* **62.13** (2007), 3378–3396.
- [5] ANSYS. *ANSYS Fluent Theory Guide*. Release 18.2. 2017.
- [6] P. A. Cundall and O. D. L. Strack. A Discrete Numerical Model for Granular Assemblies. *Geotechnique* **29** (1979), 47–65.
- [7] C. T. Crowe et al. *Multiphase flows with droplets and particles*. 2nd ed. CRC Press, 2012.
- [8] ANSYS. *Fluent Beta Features Manual*. Release 18.2. 2017.
- [9] H. Hamaker. The London – van der Waals attraction between spherical particles. *Physica IV* **10** (1937), 1058–1072.
- [10] D. Nguyen et al. Numerical modelling of breakage and adhesion of loose fine-particle agglomerates. *Chemical Engineering Sciences* **116** (2014), 91–98.
- [11] ANSYS. *ANSYS Fluent users Guide*. Release 18.2. 2017.
- [12] AIChE. *CCPS Center for Chemical Process Safety*. URL: <https://www.aiche.org/ccps/resources/glossary/process-safety-glossary/aerodynamic-diameter> (visited on 06/05/2018).
- [13] *Open Toxipedia*. 2010. URL: [https://opentoxipedia.org/index.php/Mass_Median_Aerodynamic_Diameter_\(MMAD\)](https://opentoxipedia.org/index.php/Mass_Median_Aerodynamic_Diameter_(MMAD)) (visited on 06/05/2018).
- [14] S. Dhaniyala. *Aerosol Measurement Techniques*. URL: https://webpace.clarkson.edu/projects/crcd/public_html/me637/downloads/P_Aerosol_Meas_Suresh.pdf (visited on 06/06/2018).

A Measurements

The measurements of all geometries simulated in this master's thesis work can be found in this Appendix. Two different geometries were designed to be used in the numerical simulations: the L-bend and the Ω -bend. The geometries represent the fluid domain in the numerical simulations and in the experimental testings. One additional geometry called preliminary Ω -bend was used in the computational mesh independence study.

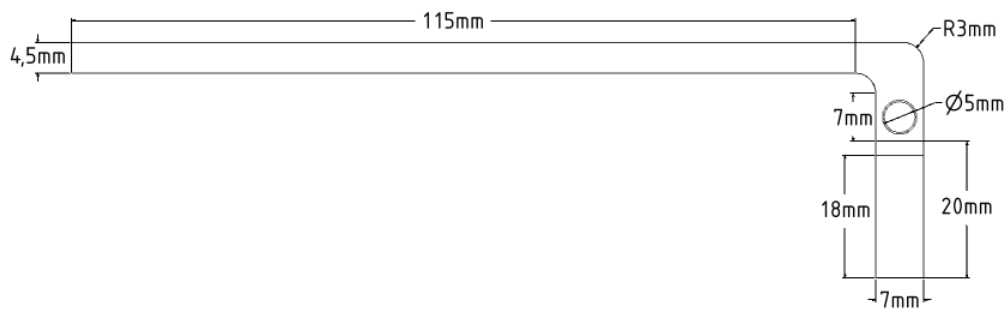


Figure A.1: Measurements of the L-bend geometry used in the simulations and experiments, seen from above with the inlet to the right.

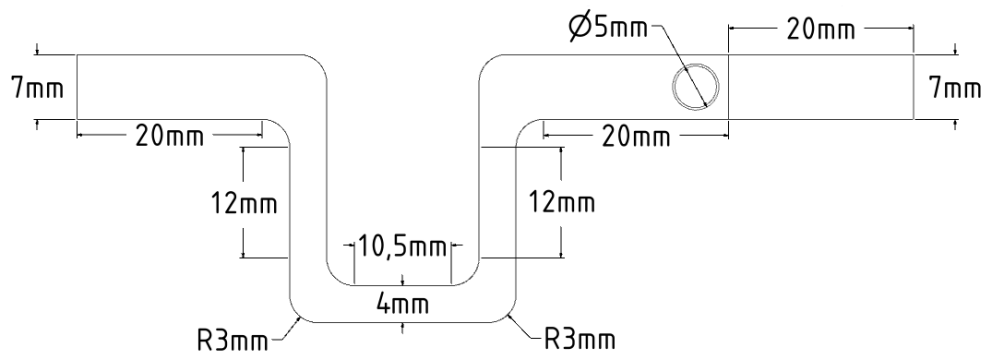


Figure A.2: Measurements of the Ω -bend geometry used in the simulations and experiments, seen from above with the inlet to the right.

A close-up of the inlet from a side view can be seen in Figure A.3 and Figure A.4.

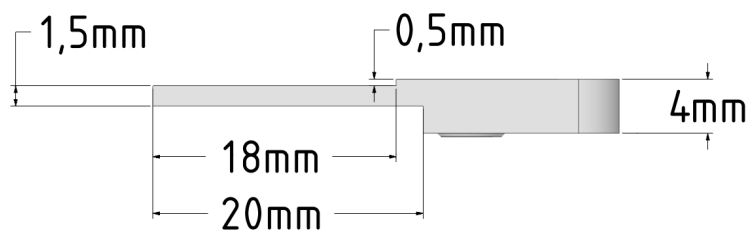


Figure A.3: Close-up of the step of the L-bend geometry seen from a lateral view, with the inlet to left.

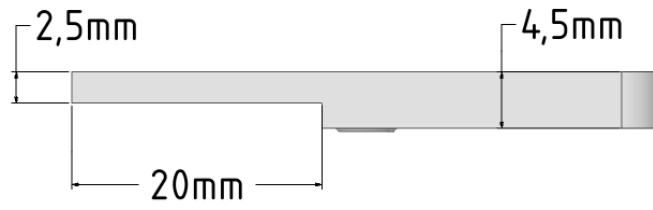


Figure A.4: Close-up of the step of the Ω -bend geometry seen from a lateral view, with the inlet to left.

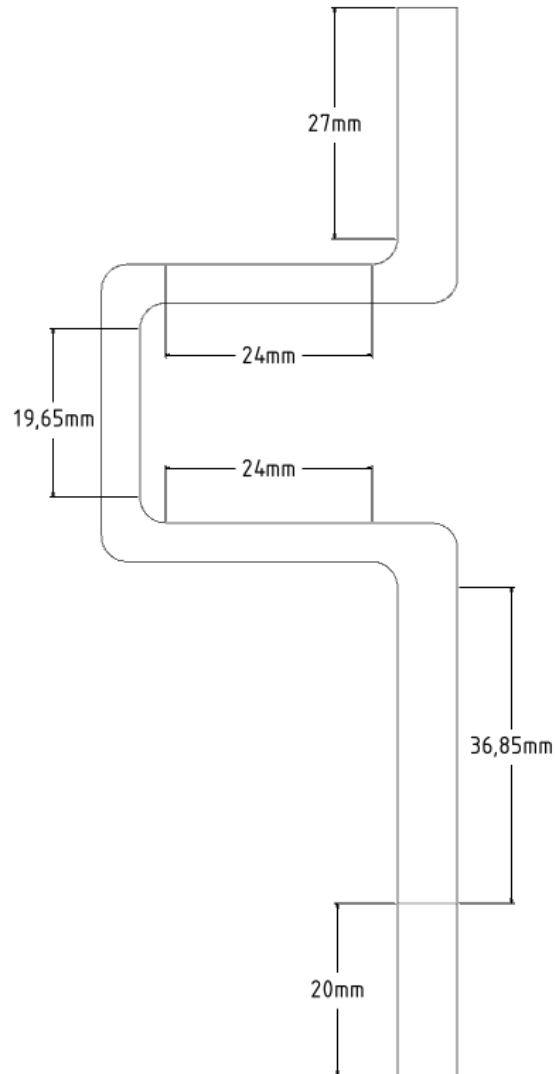


Figure A.5: Measurements of the preliminary Ω -bend geometry used in the computational mesh study, seen from above, with the inlet at the bottom.

B Experimental testing results

Complete results of the experimental testing for all devices are found in this Appendix. For the first tests on all copies, the pressure drop was not measured and this is indicated by a "-" in the tables.

Table B.1: Results for the tests on the L-bend devices.

Copy	L1			L2			L3		
Test nr	1	2	3	4	5	6	7	8	9
Loaded drug dose [mg]	4.6	10.7	8.9	5.2	9.9	7.9	10	8.3	9.7
Dose of fine particles [μg]	184	428	356	208	396	316	400	332	388
FFE	0.50	0.26	0.27	0.64	0.23	0.41	0.45	0.43	0.47
Retained dose [mg]	0.3	1.4	2.1	0	1.3	1.7	2.5	1.2	2.2
RDF	0.07	0.13	0.27	0.00	0.13	0.22	0.25	0.15	0.23
MMAD [μm]	1.84	1.86	2.05	1.8	1.92	1.84	1.81	1.83	1.85
Pressure drop [kPa]	-	3.85	3.96	-	3.49	3.66	-	3.42	3.26

Table B.2: Results for the tests on the Ω -bend devices.

Copy	$\Omega 1$			$\Omega 2$			$\Omega 3$		
Test nr	1	2	3	4	5	6	7	8	9
Loaded drug dose [mg]	7.1	7.9	11.1	6.2	13.1	9.1	7	11.2	12.8
Dose of fine particles [μg]	284	316	444	248	524	364	280	448	512
FFE	0.43	0.48	0.32	0.20	0.36	0.44	0.37	0.38	0.45
Retained dose [mg]	0.35	1.6	1.2	2.1	1.5	1	1.2	0.7	0.9
RDF	0.05	0.20	0.11	0.34	0.11	0.11	0.17	0.06	0.07
MMAD [μm]	1.71	1.92	1.77	1.77	1.91	1.8	1.72	1.82	1.93
Pressure drop [kPa]	-	2.23	2.27	-	2.26	2.24	-	2.25	2.27

The following definitions apply to the entries on the left side of the columns:

Loaded drug dose	Mass of the initial loaded drug dose
Dose of fine particles	Estimated mass of fine particles in the initial loaded drug dose
FFE	Fine particles emitted from the device divided by the initial mass of fine particles
Retained dose	Mass of the drug powder retained in the device
RDF	Ratio of the drug powder retained in the device to the the initial loaded drug dose
MMAD	Mass median aerodynamic diameter of emitted particles
Pressure drop	Pressure drop measured over the device